



Available online at www.sciencedirect.com

ScienceDirect

Comput. Methods Appl. Mech. Engrg. 387 (2021) 114182

Computer methods in applied mechanics and engineering

www.elsevier.com/locate/cma

Asynchronous phase field fracture model for porous media with thermally non-equilibrated constituents

Hyoung Suk Suha, WaiChing Sunb,*

a Department of Civil Engineering and Engineering Mechanics, 610 SW Mudd Columbia University, New York, NY 10027, United States of America

^b Department of Civil Engineering and Engineering Mechanics, Columbia University, 614 SW Mudd, Mail Code: 4709, New York, NY 10027, United States of America

> Received 8 April 2021; received in revised form 19 August 2021; accepted 7 September 2021 Available online 5 October 2021

Abstract

This paper presents the mathematical framework and the asynchronous finite element solver that captures the brittle fractures in multi-phase fluid-infiltrating porous media at the mesoscale where the constituents are not necessarily in a thermal equilibrium state. To achieve this goal, we introduce a dual-temperature effective medium theory in which the distinct constituent temperatures are homogenized independently whereas the heat exchange among the constituents is captured via phenomenological heat exchange laws in analog to the dual-permeability theory. To handle the different growth rates of the boundary layers in a stable and computationally efficient manner, an asynchronous time integrator is proposed and implemented in an operator-split algorithm that updates the displacement, pore pressure, phase field, and temperature of each constituent in an asynchronous manner. Numerical examples are introduced to verify the implementation and compare the path-dependent behaviors predicted by the dual-temperature and one-temperature models.

© 2021 Elsevier B.V. All rights reserved.

Keywords: Local thermal non-equilibrium; Brittle fracture; Porous media; Hydraulic fracture

1. Introduction

The thermo-hydro-mechanical responses of porous media are critical for many geothermal and geomechanics applications such as underground radioactive waste disposal, geothermal energy recovery, oil production, and CO₂ geological storage [1–9]. For instance, frictional heating may lead to the temperature increase of both the solid skeleton and the pore fluid through heat exchanges [10]. Geological storage of CO₂ and oil recovery often require the injection of the pore fluid in a supercritical state such that the thermal convection may play an important role both for the fluid transport and the fluid-driven fracture. The combination of temperature, pressure, and loading rate are also critical for the brittle–ductile transition of geological materials [11–13]. Heat exchange is an important mechanism for selecting the candidate materials for the nuclear waste geological disposal such as clay and salt. Long-term disposal such as the Yucca Mountain Project in New Mexico, for instance, relies on the combination of

^{*} Corresponding author.

E-mail address: wsun@columbia.edu (W. Sun).

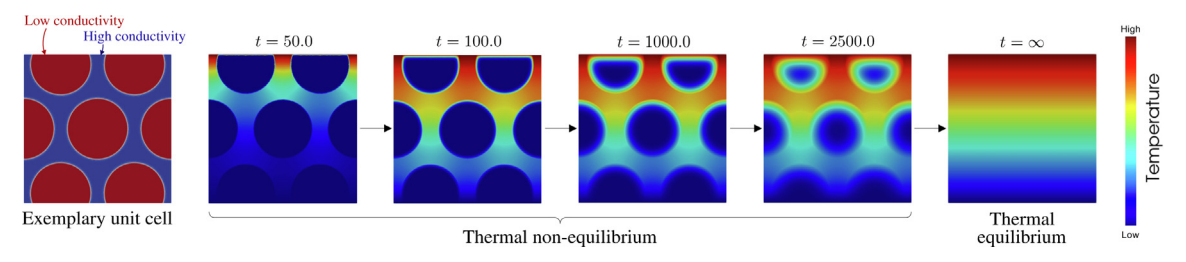


Fig. 1. Longitudinal heat transfer on an exemplary unit cell that consists of two different materials with different thermal conductivities.

low permeability, high thermal conductivity, and self-healing mechanisms to ensure the isolation of the radioactive wastes [14–16].

Traditionally, large-scale reservoir simulators that simulate thermo-hydro-mechanical responses of porous media, such as TOUGH-FLAC [17] and OpenGeoSys [18], often assume that different constituents of the porous media share the same temperature. This assumption could be valid when (1) the representative elementary volume is sufficiently large for the macroscopic porous continua to function as an effective medium for the multiphase materials, and (2) when the time scale considered in the simulations is much larger than the time it takes for the constituents to reach equilibrium locally. This assumption may lead to discrepancy to experimental observation when the constituents have significant difference in specific heat capacity and thermal conductivity, and when the temporal and spatial scales of interest are sufficiently small such that the "homogenized" temperature may yield erroneous results that violate the thermodynamic principle [19–28].

As a thought experiment, we construct a heat conduction problem of which the domain is occupied by a twophase material where the host matrix exhibits four orders higher thermal conductivity than that of the inclusion. As demonstrated in Fig. 1, this leads to a period of transition in which the heat transfer among the constituents dominates the overall thermal responses. While it is possible to obtain effective thermal conductivity through homogenization, doing so may not be suitable to capture the thermo-hydro-mechanical responses where the difference in the thermal expansion among the constituents and the thermal-softening of the solid skeleton may both affect the residual stress of the constituents. This issue has also been captured in experiments. For example, Truong and Zinsmeister [29] showed that the one-temperature approach may not yield physically consistent results if thermal conductivities of the constituent differ significantly, which corroborates our simulation in Fig. 1, while He et al. [30] pointed out that the local thermal equilibrium assumption is only valid when the interstitial heat transfer coefficient between the constituents is sufficiently large or the specific surface area of the porous medium is high enough. Furthermore, Jiang et al. [31] showed that the effect of local thermal non-equilibrium becomes more significant in fractured media where the convective heat flow inside the fracture plays a crucial role in its coupled behavior. Accordingly, it has been widely recognized that the thermo-hydro-mechanical responses of the porous media can be captured more precisely for the problems at the temporal and spatial scales if the heat transfer among the constituents can be explicitly captured [32-38]. This is particularly important for strain localization and fracture simulations where small perturbations in temperature may lead to significantly different path-dependent behaviors.

Solving the thermo-hydro-mechanical problems with non-equilibrated constituents is nevertheless not trivial. Thermal convection, Soret diffusion, and the orders of difference in thermal diffusivities all require complicated and sophisticated treatments in designing the algorithm. While stabilization procedures such as streamline upwind Petrov–Galerkin (SUPG) scheme may help resolving the numerical issues related to the sharp gradient of temperature and/or pore pressure, capturing the boundary layers of multiple constituent temperature fields remain a great numerical challenge [26,39–41] and yet may have a profound impact on the brittle or quasi-brittle fracture of porous media [42–44].

The goal of this study is to fill this knowledge gap by (1) proposing a thermo-hydro-mechanical theory for deformable porous media with non-equilibrated constituents and (2) introducing an asynchronous operator-split framework that enables us to capture the coupling mechanisms among the constituents without spurious numerical oscillations or over-diffusion. To achieve the first goal, we hypothesize that the existence of an effective medium where constituents may exhibit different temperature while the heat transfer among different constituents are captured by an interface constitutive law in analog with the dual-permeability theory. Meanwhile, we assume that the

material may exhibit fracture and this fracture is captured by a phase field that provides a diffusive representation of the crack location and therefore does not require embedded discontinuities. The governing equations derived from the balance principles of the solid and fluid constituents are then discretized in both spatial and time domains to establish numerical algorithm for computer simulations. In particular, we adopt the staggered scheme for the phase field fracture while enabling an asynchronous dual-temperature isothermal splitting scheme that updates the displacement, the pore pressure, the constituent temperature, and the phase field sequentially and asynchronously.

The rest of the paper is organized as follows. In Section 2, we introduce the theoretical framework that enables us to consider the heat transfer among constituents in a two-phase effective medium or mixture. We present the balance principles (Section 3) and constitutive relations (Section 4) that describe the thermo-hydro-mechanically coupled behavior of fluid-saturated porous media undergoing brittle fracture. We then propose a special time integration scheme that updates the field variables in an asynchronous manner in Section 5. Finally, numerical examples are given in Section 6 to highlight the computational efficiency of the proposed scheme, and to showcase the model capacity by simulating the mechanically driven and hydraulically induced fracture propagation during the transient period where the solid and fluid constituents are thermally non-equilibrated.

As for notations and symbols, bold-faced and blackboard bold-faced letters denote tensors (including vectors which are rank-one tensors); the symbol '·' denotes a single contraction of adjacent indices of two tensors (e.g., $\mathbf{a} \cdot \mathbf{b} = a_i b_i$ or $\mathbf{c} \cdot \mathbf{d} = c_{ij} d_{jk}$); the symbol ':' denotes a double contraction of adjacent indices of tensor of rank two or higher (e.g., $\mathbb{C} : \mathbf{e} = C_{ijkl} \varepsilon_{kl}$); the symbol ' \otimes ' denotes a juxtaposition of two vectors (e.g., $\mathbf{a} \otimes \mathbf{b} = a_i b_j$) or two symmetric second-order tensors [e.g., $(\mathbf{a} \otimes \mathbf{\beta})_{ijkl} = \alpha_{ij} \beta_{kl}$]. We also define identity tensors: $\mathbf{I} = \delta_{ij}$, $\mathbb{I} = \delta_{ik} \delta_{jl}$, and $\mathbb{I} = \delta_{il} \delta_{jk}$, where δ_{ij} is the Kronecker delta. As for sign conventions, unless specified, the directions of the tensile stress and dilative pressure are considered as positive.

2. Modeling approaches

In this section, we introduce the necessary ingredients for the conservation laws and the constitutive relations that will be presented later in Sections 3 and 4. We first present the homogenization strategy for the solid and fluid temperatures that allows us to consider non-isothermal effects in a two-phase porous medium with thermally non-equilibrated constituents. Kinematic assumptions based on the mixture theory are also stated, where thermal expansion of the solid skeleton is considered to be isotropic and solely depends on the solid temperature. We then summarize the smooth approximation of crack topology that adopts an implicit function, in which the phase field variable serves as a damage parameter while the regularization length scale parameter controls the size of the diffusive crack zone. Based on this setting, we define the effective stress by following the scenario from [45], which decomposes the free energy functional into multiple parts including the effective strain energy stored in the solid skeleton and the energy stored in the pore fluid.

2.1. Kinematics and homogenization strategy

Consider a fully saturated porous element Ω composed of solid (s) and fluid (f) constituents, i.e., $\Omega = \overline{\Omega_s \cup \Omega_f}$. In small scale, the spatial distribution of each constituent in Ω can be represented by indicator functions $r^s(y)$ and $r^f(y)$:

$$r^{s}(\mathbf{y}) = \begin{cases} 1 & \text{if } \mathbf{y} \in \Omega_{s}, \\ 0 & \text{otherwise,} \end{cases}; \quad r^{f}(\mathbf{y}) = \begin{cases} 1 & \text{if } \mathbf{y} \in \Omega_{f}, \\ 0 & \text{otherwise,} \end{cases}$$
(1)

where y denotes the position vector associated with small-scale configuration. By assuming that Ω can be regarded as a representative volume element (RVE), the mixture theory states that the material of interest can be idealized as a homogenized continuum mixture \mathcal{B} in which the solid and fluid constituents occupy a fraction of volume at the same material point \mathcal{P} [46–48]. In this case, the volume fractions of each phase constituent are defined as,

$$\phi^s = \frac{dV_s}{dV} = \frac{1}{dV} \int_{\Omega} r^s(\mathbf{y}) d\Omega \; ; \; \phi^f = \frac{dV_f}{dV} = \frac{1}{dV} \int_{\Omega} r^f(\mathbf{y}) d\Omega, \tag{2}$$

where $dV = \int_{\Omega} [r^s(y) + r^f(y)] d\Omega$ indicates the total elementary volume of the mixture, such that $\phi^s + \phi^f = 1$. Similarly, the total mass of the mixture at \mathcal{P} is defined by the mass from each constituent, i.e., $dM = dM_s + dM_f$,

and the intrinsic mass densities for the *i*-phase are given by $\rho_i = dM_i/dV_i$. Hence, the total mass density of the mixture reads,

$$\rho = \rho^s + \rho^f = \phi^s \rho_s + \phi^f \rho_f, \tag{3}$$

where $\rho^i = dM_i/dV$ is the partial mass density for the *i*-phase constituent.

While previous studies on thermo-hydro-mechanics often employ a single temperature field at meso- or macroscales (θ_m) [23–28], this study adopts a different homogenization strategy for each constituent. This approach not only allows us to model detailed non-isothermal processes in porous media but also to avoid the need to construct the mapping between small- and large-scale temperature fields. Having defined the indicator functions in Eq. (1), we define the intrinsic large-scale solid and fluid temperatures (θ_s and θ_f , respectively) as follows:

$$\theta_s = \frac{1}{dV_s} \int_{\Omega} r^s(\mathbf{y}) \theta(\mathbf{y}) d\Omega \; ; \; \theta_f = \frac{1}{dV_f} \int_{\Omega} r^f(\mathbf{y}) \theta(\mathbf{y}) d\Omega, \tag{4}$$

where $\theta(y)$ is the small-scale temperature field. Here, if the solid and fluid temperatures at the same material point are different from each other, the constituents are said to be in local thermal non-equilibrium (LTNE), where the heat exchange between two phases should be taken into account [36,37,49–51]. On the other hand, for the case where two temperatures are identical to each other at the same material point, two constituents are said to be in local thermal equilibrium (LTE), implying a zero heat exchange between the phases. Note that the previous works that adopt a single temperature field (i.e., one-temperature model) often rely on the assumption that the solid and fluid temperatures reach a local equilibrium instantly (i.e., $\theta_s = \theta_f = \theta_m$). In this case, the homogenized large-scale temperature θ_m may no longer depend on the volume fraction of the constituents nor their microstructural attributes, i.e.,

$$\theta_m = \frac{1}{dV} \int_{\Omega} \theta(\mathbf{y}) \, d\Omega. \tag{5}$$

For the kinematic assumptions, we follow the classical theory of porous media [52–56] and directly adopt the macroscopic descriptions. Specifically, we assume that the solid constituent forms a deformable skeletal structure (i.e., solid skeleton or solid matrix) at the RVE scale so that the evolution of our target porous material can be described in terms of the deformation of its solid skeleton. Since this study considers distinctive temperature fields for each phase constituents, the volume-averaged thermal expansion of the constituents is not used to compute thermal expansion of the porous medium [57–59]. Instead, we assume that the solid skeleton is linear thermoelastic, while the thermal expansion of solid skeleton solely depends on the solid temperature θ_s . Considering a body of two-phase continuum mixture \mathcal{B} with material points identified by the large-scale position vectors $\mathbf{x} \in \mathcal{B}$, we denote the displacement of the solid skeleton by $\mathbf{u}(\mathbf{x},t)$ at time t, so that the strain measure $\boldsymbol{\varepsilon}$ can be defined as follows:

$$\boldsymbol{\varepsilon} = \boldsymbol{\varepsilon}^e + \boldsymbol{\varepsilon}^{\theta_s} = \frac{1}{2} \left(\nabla \boldsymbol{u} + \nabla \boldsymbol{u}^{\mathrm{T}} \right), \tag{6}$$

where $\boldsymbol{\varepsilon}^e$ is the elastic component of the strain tensor and $\boldsymbol{\varepsilon}^{\theta_s} = \alpha_s(\theta_s - \theta_{s,\text{ref}})\boldsymbol{I}$ is its thermal component, where $\theta_{s,\text{ref}}$ is the reference temperature and α_s is the linear thermal expansion coefficient of the solid constituent. Notice that, as pointed out in [60], the linear thermal expansion coefficient of the solid skeleton is solely controlled by and is equivalent to that of solid phase constituent. In other words, by revisiting the homogenization strategy in Eq. (4), it implies that the macroscopic temperature of the solid phase θ_s can be considered to be equivalent to that of solid skeleton.

2.2. Phase field approximation of crack topology

This study adopts the diffuse representation of fracture by using the phase field approach [42,43,61]. By letting Γ be the sharp crack surface within a body of mixture \mathcal{B} , the total fracture surface area A_{Γ} can be approximated as A_{Γ_d} , which is the volume integral over body \mathcal{B} of the surface density $\Gamma_d(d, \nabla d)$. In other words,

$$A_{\Gamma} \approx A_{\Gamma_d} = \int_{\mathcal{B}} \Gamma_d (d, \nabla d) \ dV, \tag{7}$$

where $d \in [0, 1]$ is the phase field that serves as a damage parameter in which d = 0 indicates the intact region while d = 1 denotes the completely damaged region. Here, the approximation A_{Γ_d} must be able to recover A_{Γ} by

reducing the regularization length scale parameter l_c to zero (i.e., Γ -convergence), while the generalized form of the corresponding crack density functional [62] reads,

$$\Gamma_d(d, \nabla d) = \frac{1}{c_0} \left[\frac{1}{l_c} w(d) + l_c \left(\nabla d \cdot \nabla d \right) \right] \; ; \; c_0 = 4 \int_0^1 \sqrt{w(s)} \, ds, \tag{8}$$

where c_0 is the normalization constant, and w(d) is the monotonically increasing local dissipation function that controls the shape of the regularized profile of the phase field [63–65]. Note that a linear local dissipation along with a quadratic stiffness degradation yields a threshold energy model (existence of a linear elastic phase before the onset of damage), which is contrary to the quadratic model for which damage starts at zero loading. However, the threshold energy model can be converted to a critical stress which is dependent of the length scale parameter l_c . Both approaches have been used to model brittle fracture as two alternative regularizations of the variational theory of brittle fracture of Francfort and Marigo [66]. Meanwhile, previous work, such as [44,67–69], have used non-quadratic degradation function which may yield a critical stress independent of l_c .

In this study, we adopt the quadratic local dissipation model, so that the crack resistance force \mathcal{R}^c can be expressed as [70]:

$$\mathcal{R}^{c} = \frac{\partial W^{c}}{\partial d} - \nabla \cdot \left(\frac{\partial W^{c}}{\partial \nabla d}\right); \quad W^{c} = \mathcal{G}_{c} \Gamma_{d} (d, \nabla d) = \frac{\mathcal{G}_{c}}{l_{c}} \left[\frac{d^{2}}{2} + \frac{l_{c}^{2}}{2} (\nabla d \cdot \nabla d)\right], \tag{9}$$

where $G_c = G_c(\theta_s)$ is the critical energy release rate that quantifies the resistance to cracking, which will be explicitly defined in Section 4.2.

2.3. Free energy and effective stress principle

We adopt the effective stress principle that decomposes the total macroscopic stress σ into the effective stress σ' and the contribution due to the pore fluid pressure p_f . As the effective stress is solely caused by the macroscopic deformation of the solid skeleton, it constitutes an energy-conjugate relationship with the strain measure [71,72]. As such, the free energy (ψ) of the porous media may take the following form (cf. [45]):

$$\psi = \psi'(\boldsymbol{\varepsilon}, \theta_{s}, d) + \psi^{*}(\boldsymbol{\varepsilon}, \vartheta^{*}, d) + \psi^{\theta_{s}}(\theta_{s}) + \psi^{\theta_{f}}(\theta_{f}). \tag{10}$$

Note that the energy required for crack growth [i.e., W^c in Eq. (9)] is dissipative by nature and hence not included in this stored energy function ψ [13,41,70]. Our definition of free energy will be used for constructing the energy balance equations based on the first law of thermodynamics in Section 3.1, while this section defines all the terms in detail first, and then presents the effective stress principle.

The effective part of the strain energy density $\psi'(\varepsilon, \theta_s, d)$ can be viewed as a stored energy density due to the intergranular stress acting on the solid skeleton that leads to its deformation. In particular, we assume that the effective part of the strain energy density $\psi'(\varepsilon, \theta_s, d)$ is composed of the fictitious undamaged thermoelastic strain energy $\psi'_0(\varepsilon, \theta_s)$ and the degradation function $g(d) \in [0, 1]$ [15,73,74], i.e.,

$$\psi'(\boldsymbol{\varepsilon}, \theta_s, d) = g(d)\psi'_0(\boldsymbol{\varepsilon}, \theta_s) \; ; \; \psi'_0(\boldsymbol{\varepsilon}, \theta_s) = \frac{1}{2}\boldsymbol{\varepsilon} : \mathbb{C}^e : \boldsymbol{\varepsilon} - 3\alpha_s K(\theta_s - \theta_{s, \text{ref}}) \operatorname{tr}(\boldsymbol{\varepsilon}), \tag{11}$$

where \mathbb{C}^e is the elastic moduli and K is the bulk modulus of the solid skeleton. This approach allows us to interpret the cracking in a saturated porous material as the fracture of the solid matrix.

Following Miehe and Mauthe [45], and by assuming that the effect of thermal expansion of the pore fluid is negligible (i.e., its thermal expansion coefficient $\alpha_f = 0$), the contribution of pore fluid to the free energy $\psi^*(\varepsilon, \vartheta^*, d)$ can be defined as follows:

$$\psi^*(\boldsymbol{\varepsilon}, \vartheta^*, d) = \frac{1}{2} M^*(d) \left[B^*(d) \operatorname{tr}(\boldsymbol{\varepsilon}) - \vartheta^* \right]^2 \; ; \; \vartheta^* = B^*(d) \operatorname{tr}(\boldsymbol{\varepsilon}) + \frac{p_f}{M^*(d)}, \tag{12}$$

where the expression for ϑ^* is similar to Eq. (2.12) in [75], while $B^*(d)$ and $M^*(d)$ are the modified Biot's coefficient and the modified Biot's modulus, respectively:

$$B^*(d) = 1 - \frac{K^*(d)}{K_s} \; ; \; \frac{1}{M^*(d)} = \frac{B^*(d) - \phi^f}{K_s} + \frac{\phi^f}{K_f}. \tag{13}$$

Here, $K^*(d) = g(d)K$, while K_s and K_f denote the bulk moduli of the solid and fluid phases, respectively. As shown in Eq. (13), this study assumes that the damage of the solid skeleton degrades the elastic bulk modulus $K^*(d)$, so that $B^*(d)$ and $M^*(d)$ may evolve according to the deformation. In other words, if the solid skeleton remains undamaged, the modified coefficient recovers the classical definition of Biot's coefficient (i.e., $B^* = 1 - K/K_s$) that is often less than 1 for rock [23,76,77], while we have $B^*(1) = 1$ for the case where the solid skeleton is completely damaged, which has been accepted in previous studies on hydraulic fracture [45,78,79]. Following Heider and Sun [80], we assume that crack opening leads to a complete fragmentation of solid skeleton, such that we adopt the following relation for the porosity (i.e., the volume fraction of fluid phase constituent ϕ^f):

$$\phi^f = 1 - g(d)(1 - \phi_{ref}^f)(1 - \nabla \cdot \boldsymbol{u}),\tag{14}$$

where ϕ_{ref}^f is the reference porosity. We also define $\varphi = \vartheta^* - B^*(d) \operatorname{tr}(\boldsymbol{\varepsilon})$ for convenience, which is related to the variation of the fluid content and is the energy conjugate to the pore fluid pressure p_f . In this case, Eq. (12) can be re-written in a simple quadratic form:

$$\psi^*(\boldsymbol{\varepsilon}, \vartheta^*, d) = \psi^*(\varphi, d) = \frac{1}{2} M^*(d) \varphi^2. \tag{15}$$

The pure thermal contribution on the stored energy density $\psi^{\theta_i}(\theta_i)$ may have the simple form as [15,73,74,81],

$$\psi^{\theta_i}(\theta_i) = \rho^i c_i \left[(\theta_i - \theta_{i,ref}) - \theta_i \ln \left(\frac{\theta_i}{\theta_{i,ref}} \right) \right], \tag{16}$$

where $i = \{s, f\}$, while c_i indicates the specific heat capacity and $\theta_{i,ref}$ is the reference temperature for the i-phase constituent. Note that, as shown in Eq. (16), we simplify the coupled thermo-mechanical-fracture problem by assuming that the thermal part of the stored energy densities $\psi^{\theta_s}(\theta_s)$ and $\psi^{\theta_f}(\theta_f)$ are not affected by the fracture (cf. [15,45,70]).

Having defined all the terms for the free energy, we now present the effective stress principle based on the hyperelastic relations. From Eqs. (10), (11), and (12), the total stress σ can be found by taking the partial derivative of the total energy density ψ with respect to the strain ϵ :

$$\sigma = \frac{\partial \psi}{\partial \varepsilon} = \underbrace{\frac{\partial}{\partial \varepsilon} \psi'(\varepsilon, \theta_s, d)}_{=\sigma'} + \underbrace{\frac{\partial}{\partial \varepsilon} \psi^*(\varepsilon, \vartheta^*, d)}_{=-B^*(d)p_f I}.$$
(17)

A similar decomposition can be found in a number of studies on theories of porous media [52–56], where the first term on the right hand side in Eq. (17) becomes the effective stress σ' , while the second term indicates the contribution of the pore pressure which is assumed to produce a hydrostatic stress state [45]. From Eqs. (11) and (17), the effective stress tensor can also be expressed as,

$$\sigma' = \sigma + B^*(d)p_f I = g(d)\sigma'_0, \tag{18}$$

where $\sigma_0' = \partial \psi_0' / \partial \varepsilon$ is the fictitious undamaged effective stress.

3. Conservation laws for thermally non-equilibrated porous media

In this section, we derive the balance principles that govern the brittle fracture in saturated porous media with constituents of different temperatures. While previous work such as [15,28,74,82] has introduced a framework to address the thermal effect of brittle or quasi-brittle fracture in porous media, our new contribution here is to introduce the heat exchange between the two thermally connected constituents, such that the multi-scale nature of the heat transfer can be considered. Since our homogenization strategy enables us to consider two macroscopic temperatures for each constituent, we derive two distinct energy balance equations by assuming that the thermodynamic state of each phase is measured by their own temperature, internal energy, and entropy. Our derivation in Section 3.1 shows that the two-temperature approach can be reduced into a classical heat equation with a single temperature field if we consider the special case where two constituents are thermally equilibrated. Then, in addition to two energy equations, we present a thermodynamically consistent phase field model and the balances of linear momentum and mass, that complete the set of governing equations which not only describes the thermo-hydro-mechanical behavior of porous media in local thermal non-equilibrium, but also the evolution of the fracture.

3.1. Balance of energy

In contrast to the models that employ a single temperature field [21,24,27], our approach requires two energy balance equations for each phase in order to account for the transient period, i.e., local thermal non-equilibrium [36,37,83]. Hence, following Gelet et al. [83], we assume that thermodynamic states of the solid skeleton and pore fluid can respectively be measured by their own temperature θ_i , internal energy E_i and entropy H_i per unit mass. Based on the assumption, the internal energy per unit volume e can additively be decomposed as follows,

$$e = e^s + e^f ; \quad e^i = \rho^i E_i, \tag{19}$$

where $i = \{s, f\}$ so that e^i is the partial quantity. Similarly, entropy per unit volume of the mixture η can also be decomposed into,

$$\eta = \eta^s + \eta^f \; ; \; \eta^i = \rho^i H_i, \tag{20}$$

where we assume that each partitioned entropies satisfy:

$$\eta^i = -\frac{\partial \psi^i}{\partial \theta_i}.\tag{21}$$

Here, by revisiting Section 2.3, we define ψ^i as,

$$\psi = \psi^s + \psi^f \; ; \; \begin{cases} \psi^s = \psi'(\boldsymbol{\varepsilon}, \theta_s, d) + \psi^{\theta_s}(\theta_s), \\ \psi^f = \psi^*(\varphi, d) + \psi^{\theta_f}(\theta_f), \end{cases}$$
 (22)

such that ψ^s and ψ^f are the partial free energy of the solid and fluid phase constituents, respectively. As shown in Eq. (22), this study assumes that the effects of the skeletal structure of the solid phase (e.g., effective stress and degradation) on the free energy is solely stored in ψ^s , while ψ^f only includes the contribution of its intrinsic pressure and temperature. Furthermore, we postulate that the partial quantities of internal energy e^i and entropy η^i can be subjected to a Legendre transformation, i.e.,

$$\psi^i = e^i - \theta_i \eta^i, \tag{23}$$

so that the following classical relation [84–86] can be recovered if two constituents are in thermal equilibrium (i.e., $\theta_s = \theta_f = \theta_m$):

$$\psi = \sum_{i=\{s,f\}} \psi^i = \sum_{i=\{s,f\}} (e^i - \theta_i \eta^i) = e - \theta_m \eta.$$
(24)

On the other hand, the energy exchange between the constituents can be described by introducing the rates of energy transfer χ^i , in which energy conservation requires the following constraint to be satisfied:

$$\chi^s + \chi^f = 0. ag{25}$$

Based on the first law of thermodynamics, the balance of energy for the solid constituent that accounts for the flux of thermal energy due to heat conduction (q^s) , the rate of energy exchange (χ^s) , and the heat source (\hat{r}^s) can be written as,

$$\dot{\boldsymbol{e}}^{s} = \boldsymbol{\sigma}' : \dot{\boldsymbol{e}} - \nabla \cdot \boldsymbol{q}^{s} + \boldsymbol{\chi}^{s} + \hat{\boldsymbol{r}}^{s}, \tag{26}$$

where $(\bullet) = d(\bullet)/dt$ is the total material time derivative following the solid phase. Although will be discussed later in Section 3.2, we briefly show that the second law of thermodynamics (i.e., Clausius–Duhem inequality) yields the following expression for the dissipation functional \mathcal{D}^s :

$$\mathcal{D}^{s} = \left(\boldsymbol{\sigma}' - \frac{\partial \psi^{s}}{\partial \boldsymbol{\varepsilon}}\right) : \dot{\boldsymbol{\varepsilon}} - \left(\eta^{s} + \frac{\partial \psi^{s}}{\partial \theta_{s}}\right) \dot{\theta}_{s} \underbrace{-\frac{\partial \psi^{s}}{\partial d} \dot{d}}_{=\mathcal{D}^{s}_{\text{int}}} \underbrace{-\frac{1}{\theta_{s}} \boldsymbol{q}^{s} \cdot \nabla \theta_{s}}_{=\mathcal{D}^{s}_{\text{con}}} \ge 0, \tag{27}$$

where the entropy input is assumed to be related to the heat flux across the boundary and the heat source [15,82]. From the relations defined previously [Eqs. (17) and (21)], dissipation functional in Eq. (27) can be reduced into,

$$\mathcal{D}^s = \mathcal{D}^s_{\text{int}} + \mathcal{D}^s_{\text{con}} \ge 0. \tag{28}$$

Finally, from Eqs. (23) and (26), the solid phase energy balance equation in Eq. (26) becomes:

$$\dot{\psi}^s - \dot{e}^s + \frac{\dot{\sigma}_s}{\theta_s \eta^s} = \theta_s \dot{\eta}^s - \mathcal{D}_{int}^s + \nabla \cdot \boldsymbol{q}^s - \chi^s - \hat{r}^s = 0. \tag{29}$$

By substituting the explicit expression for η^s [i.e., from Eqs. (20) and (22)], Eq. (29) can be re-written as follows, where similar form can be found in [15,26,87].

$$\rho^s c_s \dot{\theta}_s = (\mathcal{D}_{int}^s - H_{\theta_s}) - \nabla \cdot \boldsymbol{q}^s + \chi^s + \hat{r}^s. \tag{30}$$

In this study, to simplify the equation, we assume that structural heating/cooling is negligible (i.e., $H_{\theta_s}=0$) compared to the internal dissipation \mathcal{D}_{int} .

We now repeat the same procedure for the fluid phase. Again, from the first law, the internal energy for the pore fluid that accounts for the heat flux due to the conduction (q^f) , the rate of energy exchange (χ^f) , the heat convection (\mathcal{A}^f) , and the heat source (\hat{r}^f) can be written as,

$$\dot{e}^f = -p_f \dot{\varphi} - \mathcal{A}^f - \nabla \cdot \mathbf{q}^f + \chi^f + \hat{r}^f, \tag{31}$$

where we take $\mathcal{A}^f = \rho_f c_f(\boldsymbol{w} \cdot \nabla \theta_f)$ with \boldsymbol{w} denoting Darcy's velocity, by assuming that the advection process is governed by the movement of the pore fluid relative to that of the solid skeleton [25,83]. Recall that from Eqs. (12), (15) and (21) we have: $p_f = -M^* \varphi$ and $\eta^f = -\partial \psi^f / \partial \theta_f$. Thus, from Eqs. (23) and (31), the fluid energy balance equation reads,

$$\dot{\psi}^f - \dot{e}^f + \frac{\dot{\sigma}}{\theta_f \eta^f} = \theta_f \dot{\eta}^f + \mathcal{A}^f + \nabla \cdot \boldsymbol{q}^f - \chi^f - \hat{r}^f, \tag{32}$$

where we assume that the contribution of the phase field on ψ^f is negligible. Then, by substituting the explicit expression for η^f , the fluid phase energy balance equation can be re-written as,

$$\rho^f c_f \dot{\theta}_f = -\rho_f c_f(\mathbf{w} \cdot \nabla \theta_f) - \nabla \cdot \mathbf{q}^f + \chi^f + \hat{r}^f, \tag{33}$$

where Eq. (33) is similar to the form that seen in [88–90].

Remark 1. Eqs. (30) and (33) describe the heat transfer process in porous media under LTNE condition, however, one may obtain a different form of governing equations if adopting either different form of the free energy functional or different decomposition scheme on the internal energy. Based on our approach, for the situation where the material is undamaged (d = 0) and is under LTE condition (i.e., $\theta_s = \theta_f = \theta_m$), adding Eqs. (30) and (33) yields the classical one-temperature model [21,23,24,55]:

$$\rho c_m \dot{\theta}_m = -\rho_f c_f(\boldsymbol{w} \cdot \nabla \theta_m) - \nabla \cdot \boldsymbol{q} + \hat{r}, \tag{34}$$

where $\rho c_m = \rho^s c_s + \rho^f c_f$, $q = q^s + q^f$, and $\hat{r} = \hat{r}^s + \hat{r}^f$. Here, Eq. (34) not only demonstrates the connection between one- and two-temperature approaches but also implies that the classical model assumes a special case where all the phase constituents instantly reach a local thermal equilibrium.

3.2. Dissipation inequality and crack evolution

By revisiting the expression for the dissipation functional \mathcal{D}^s in Eq. (28), the following thermodynamic restriction must be satisfied:

$$\mathcal{D}_{\text{int}}^s = \mathcal{F}^c \dot{d} \ge 0,\tag{35}$$

since the dissipation due to heat conduction $\mathcal{D}^s_{\mathrm{con}}$ is guaranteed positive by the Fourier's law, while:

$$\mathcal{F}^c = -\frac{\partial \psi^s}{\partial d} = -g'(d)\psi_0' \tag{36}$$

indicates the crack driving force [70,82]. Notice that a sufficient condition for the inequality in Eq. (35) is that all the components \mathcal{F}^c and \dot{d} are individually non-negative. By adopting the quadratic degradation function, i.e., $g(d) = (1-d)^2$, that satisfies the following conditions [44,91]:

$$g(0) = 1 \; ; \; g(1) = 0 \; ; \; g'(d) \le 0 \text{ for } d \in [0, 1],$$
 (37)

the non-negative crack driving force \mathcal{F}^c is automatically guaranteed since $\psi'_0 \ge 0$. In this case, the thermodynamic restriction in Eq. (35) becomes:

$$\dot{d} \ge 0. \tag{38}$$

While the stored energy functional in the microforce approach often contains the fracture energy [15,92,93], recall Section 2.3 that our energy functional ψ does not include the energy used to create a fracture. Again, it allows us to consider crack growth as a fully dissipative process, resulting in the solid phase energy balance equation [Eq. (30)] that contains the internal dissipation $\mathcal{D}_{\text{int}}^s$. Based on this setting, we adopt a concept similar to the variational framework for fracture that characterizes the crack propagation process by energy dissipation [61,66,94]. By assuming that the viscous resistance is neglected, thermodynamic consistency requires the balance between the crack driving force \mathcal{F}^c in Eq. (36) and the crack resistance \mathcal{R}^c in Eq. (9), i.e.,

$$\mathcal{R}^c - \mathcal{F}^c = g'(d)\psi_0' + \frac{\mathcal{G}_c}{l_c}(d - l_c^2 \nabla^2 d) = 0,$$
(39)

where $\nabla^2(\bullet) = \nabla \cdot \nabla$ (\bullet) indicates the Laplacian operator. Here, we adopt the volumetric-deviatoric split proposed by Amor et al. [95], which is the stored energy that may contribute as the driving force for crack growth, i.e.,

$$\psi_0^{\prime +} = \frac{1}{2} \langle \varepsilon^{\text{vol}} \rangle_+^2 + \mu(\boldsymbol{\varepsilon}^{\text{dev}} : \boldsymbol{\varepsilon}^{\text{dev}}) - 3\alpha_s K(\theta_s - \theta_{s,\text{ref}}) \langle \varepsilon^{\text{vol}} \rangle_+, \tag{40}$$

$$\psi_0^{\prime -} = \frac{1}{2} \langle \varepsilon^{\text{vol}} \rangle_{-}^2 - 3\alpha_s K(\theta_s - \theta_{s,\text{ref}}) \langle \varepsilon^{\text{vol}} \rangle_{-}, \tag{41}$$

where $\varepsilon^{\text{vol}} = \text{tr}(\boldsymbol{\varepsilon})$, $\boldsymbol{\varepsilon}^{\text{dev}} = \boldsymbol{\varepsilon} - (\varepsilon^{\text{vol}}/3)\boldsymbol{I}$, and $\langle \bullet \rangle_{\pm} = \langle \bullet \pm | \bullet | \rangle/2$ indicates the Macaulay bracket operator. To prevent healing of the crack, we adopt a normalized local history field $\mathcal{H} \geq 0$ of the maximum positive reference energy, i.e.,

$$\mathcal{H} = \max_{\tau \in [0,t]} \left(\frac{\psi_0^{\prime +}}{\mathcal{G}_c / l_c} \right),\tag{42}$$

which satisfies the following Karush–Kuhn–Tucker condition [13,43]:

$$W^{+} - \mathcal{H} < 0 \; ; \; \dot{\mathcal{H}} > 0 \; ; \; \dot{\mathcal{H}}(W^{+} - \mathcal{H}) = 0,$$
 (43)

where $W^+ = {\psi_0'}^+/(\mathcal{G}_c/l_c)$ denotes the portion of nondimensional ψ_0' that contributes to cracking.

By replacing the stored energy term in Eq. (39) by $(\mathcal{G}_c/l_c)\mathcal{H}$, the governing equation for the phase field d can be re-written as follows:

$$g'(d)\mathcal{H} + (d - l_c^2 \nabla^2 d) = 0. \tag{44}$$

Note that Eq. (44) is based on balance of the material force (cf. [43]) and is not a Euler-Lagrangian equation obtained from the minimization of an energy functional.

3.3. Balance of linear momentum

By neglecting the inertial force, the balance of linear momentum for the solid-fluid mixture can be written as,

$$\nabla \cdot \boldsymbol{\sigma} + \rho \boldsymbol{g} = \boldsymbol{0},\tag{45}$$

where $\sigma = \sigma^s + \sigma^f$ is the total Cauchy stress that can be obtained from the sum of partial stresses σ^i for *i*-phase constituents [96,97]. Hence, from Eq. (18), the mean pressure p can be expressed as:

$$p = -\frac{1}{3}\operatorname{tr}(\boldsymbol{\sigma}) = \phi^{s} p_{s} + \phi^{f} p_{f} = -K^{*} \nabla \cdot \boldsymbol{u} + 3\alpha_{s} K^{*}(\theta_{s} - \theta_{s, \text{ref}}) + B^{*} p_{f}, \tag{46}$$

where p_s and p_f are the intrinsic pressures defined in dV_s and dV_f , respectively, while the detailed constitutive model for the solid skeleton will be presented in Section 4.2.

3.4. Balance of mass

Assuming that there is no phase transition between two constituents, the balance of mass for the solid skeleton and the pore fluid reads,

$$\dot{\rho}^s + \rho^s \nabla \cdot \mathbf{v} = 0, \tag{47}$$

$$\dot{\rho}^f + \rho^f \nabla \cdot \mathbf{v} + \nabla \cdot \left[\rho^f (\mathbf{v}_f - \mathbf{v}) \right] = \rho_f \hat{\mathbf{s}}, \tag{48}$$

where $\rho_f \hat{s}$ is the rate of prescribed fluid mass source/sink per unit volume, while v and v_f indicate the solid and fluid velocities, respectively. Since the change of dV_s depends on both the intrinsic pressure p_s and the temperature θ_s , the total time derivative of partial density ρ^s can be expanded as,

$$\dot{\rho}^s = \frac{\dot{\sigma}}{\phi^s \rho_s} = \dot{\phi}^s \rho_s + \phi^s \left(\frac{d\rho_s}{dp_s} \dot{p}_s + \frac{d\rho_s}{d\theta_s} \dot{\theta}_s \right) = \dot{\phi}^s \rho_s + \phi^s \rho_s \left(\frac{1}{K_s} \dot{p}_s - 3\alpha_s \dot{\theta}_s \right), \tag{49}$$

so that the solid phase mass balance equation in Eq. (47) can be re-expressed as,

$$-\dot{\phi}^s = \frac{\phi^s}{K_s}\dot{p}_s - 3\alpha_s\phi^s\dot{\theta}_s + \phi^s\nabla\cdot\boldsymbol{v}. \tag{50}$$

Also, from Eq. (46), the total time derivative of mean pressure p yields:

$$\dot{p} = \overline{\phi^s p_s + \phi^f p_f} = -K^* \nabla \cdot \boldsymbol{v} + 3\alpha_s K^* \dot{\theta}_s + B^* \dot{p}_f. \tag{51}$$

Following Sun et al. [98], we assume that the change of porosity at an infinitesimal time is small (i.e., $\dot{\phi}^i p_i$ is relatively small compared to $\phi^i \dot{p}_i$), so that Eq. (51) reduces into,

$$\phi^{s} \dot{p}_{s} = -K^{*} \nabla \cdot \mathbf{v} + 3\alpha_{s} K^{*} \dot{\theta}_{s} + (B^{*} - \phi^{f}) \dot{p}_{f}. \tag{52}$$

By substituting Eq. (52) into Eq. (50), the solid phase mass balance equation now reads,

$$-\dot{\phi}^s = \frac{B^* - \phi^f}{K_s} \dot{p}_f - 3\alpha_s \left(\phi^s - \frac{K^*}{K_s}\right) \dot{\theta}_s + \left(\phi^s - \frac{K^*}{K_s}\right) \nabla \cdot \boldsymbol{v}. \tag{53}$$

Similar to Eq. (50), the fluid phase mass balance equation in Eq. (48) can also be expanded as,

$$\dot{\phi}^f + \frac{\phi^f}{K_f} \dot{p}_f - 3\alpha_f \phi^f \dot{\theta}_f + \phi^f \nabla \cdot \boldsymbol{v} + \nabla \cdot \boldsymbol{w} = \hat{s}, \tag{54}$$

where K_f is the bulk modulus of the fluid, $\mathbf{w} = \phi^f(\mathbf{v}_f - \mathbf{v})$ indicates Darcy's velocity, and α_f is the linear thermal expansion coefficient of the pore fluid which has been assumed to be zero in Section 2.3. Recall that Eq. (2) yields the condition $\phi^s + \phi^f = 1$, which leads to: $\dot{\phi}^f = -\dot{\phi}^s$. Thus, we substitute Eq. (53) into the first term in Eq. (54) that gives the following expression for the fluid phase mass balance equation:

$$\frac{1}{M^*}\dot{p}_f - 3\alpha_s(B^* - \phi^f)\dot{\theta}_s - 3\alpha_f\phi^f\dot{\theta}_f + B^*\nabla \cdot \boldsymbol{v} + \nabla \cdot \boldsymbol{w} = \hat{s}.$$
 (55)

Remark 2. If we assume that the solid and fluid temperatures are locally equilibrated (i.e., $\theta_s = \theta_f = \theta_m$) and $\hat{s} = 0$, Eq. (55) can be reduced into a similar form that is shown in [24,55,59]:

$$\frac{1}{M^*}\dot{p}_f - 3\alpha_m\dot{\theta}_m + B^*\nabla\cdot\boldsymbol{v} + \nabla\cdot\boldsymbol{w} = 0,\tag{56}$$

where $\alpha_m = (B^* - \phi^f)\alpha_s + \phi^f\alpha_f$ is the coefficient of linear thermal expansion for thermally equilibrated medium. Furthermore, if we consider a special case where thermal expansion is negligible and each constituent is incompressible (i.e., $K_i \to \infty$), Eq. (56) further reduces to the form identical to that seen in [25,98,99]:

$$\nabla \cdot \boldsymbol{v} + \nabla \cdot \boldsymbol{w} = 0, \tag{57}$$

since $B^* = 1$ and $1/M^* = 0$ in this case, regardless of the damage parameter d.

4. Constitutive responses

The goal of this section is to identify constitutive relations that capture thermo-hydro-mechanically coupled behavior of the material of interest. We begin this section by the constitutive relationships for partial heat fluxes for each phase, where we assume both the solid and fluid constituents obey Fourier's law. We also present the explicit expression for the heat exchange χ^i between the solid skeleton and pore fluid based on Newton's law of cooling. We then briefly summarize the linear thermoelasticity for the undamaged solid skeleton, while the hydraulic responses in both the bulk and crack regions are modeled by the Darcy's law, where we adopt permeability enhancement approach in order to account for the anisotropy due to the crack opening. In addition, this study adopts an empirical two-parameter model for the pore fluid viscosity, which is capable of predicting the temperature-dependent viscosity of typical liquids in geomaterials.

4.1. Thermal responses and heat exchange model

In this section, we adopt the homogenization strategy that we previously described in Section 2.1. Similar to the large-scale temperatures, by letting f(y) the small-scale heat flux vector, the large-scale heat flux q can be expressed as,

$$q = \frac{1}{dV} \int_{\Omega} f(\mathbf{y}) d\Omega = \frac{1}{dV} \int_{\Omega} \underbrace{\underbrace{r^{s}(\mathbf{y})f(\mathbf{y})}_{=f^{s}(\mathbf{y})} + \underbrace{r^{f}(\mathbf{y})f(\mathbf{y})}_{=f^{f}(\mathbf{y})} d\Omega}_{=g^{s}}$$

$$= \underbrace{\frac{dV_{s}}{dV} \left[\frac{1}{dV_{s}} \int_{\Omega} f^{s}(\mathbf{y}) d\Omega \right]}_{=q^{s}} + \underbrace{\frac{dV_{f}}{dV} \left[\frac{1}{dV_{f}} \int_{\Omega} f^{f}(\mathbf{y}) d\Omega \right]}_{=g^{f}},$$

$$= \underbrace{\frac{dV_{s}}{dV} \left[\frac{1}{dV_{s}} \int_{\Omega} f^{s}(\mathbf{y}) d\Omega \right]}_{=q^{s}} + \underbrace{\frac{dV_{f}}{dV} \left[\frac{1}{dV_{f}} \int_{\Omega} f^{f}(\mathbf{y}) d\Omega \right]}_{=g^{f}},$$

$$= \underbrace{\frac{dV_{s}}{dV} \left[\frac{1}{dV_{s}} \int_{\Omega} f^{s}(\mathbf{y}) d\Omega \right]}_{=q^{s}} + \underbrace{\frac{dV_{f}}{dV} \left[\frac{1}{dV_{f}} \int_{\Omega} f^{f}(\mathbf{y}) d\Omega \right]}_{=g^{f}},$$

$$= \underbrace{\frac{dV_{s}}{dV} \left[\frac{1}{dV_{s}} \int_{\Omega} f^{s}(\mathbf{y}) d\Omega \right]}_{=q^{s}} + \underbrace{\frac{dV_{f}}{dV} \left[\frac{1}{dV_{f}} \int_{\Omega} f^{f}(\mathbf{y}) d\Omega \right]}_{=g^{f}},$$

$$= \underbrace{\frac{dV_{s}}{dV} \left[\frac{1}{dV_{s}} \int_{\Omega} f^{s}(\mathbf{y}) d\Omega \right]}_{=q^{s}} + \underbrace{\frac{dV_{f}}{dV} \left[\frac{1}{dV_{f}} \int_{\Omega} f^{f}(\mathbf{y}) d\Omega \right]}_{=g^{f}},$$

$$= \underbrace{\frac{dV_{s}}{dV} \left[\frac{1}{dV_{s}} \int_{\Omega} f^{s}(\mathbf{y}) d\Omega \right]}_{=q^{s}} + \underbrace{\frac{dV_{f}}{dV} \left[\frac{1}{dV_{f}} \int_{\Omega} f^{s}(\mathbf{y}) d\Omega \right]}_{=g^{f}},$$

$$= \underbrace{\frac{dV_{s}}{dV} \left[\frac{1}{dV_{s}} \int_{\Omega} f^{s}(\mathbf{y}) d\Omega \right]}_{=q^{s}} + \underbrace{\frac{dV_{f}}{dV} \left[\frac{1}{dV_{f}} \int_{\Omega} f^{s}(\mathbf{y}) d\Omega \right]}_{=g^{f}},$$

so that $q = q^s + q^f$. For the constitutive model that describes the heat conduction, we assume that both the solid and fluid constituents obey the Fourier's law, such that their partial heat flux q^i ($i \in \{s, f\}$) can be written as,

$$\boldsymbol{q}^{i} = \phi^{i} \boldsymbol{q}_{i} = -\phi^{i} \kappa_{i} \nabla \theta_{i}, \tag{59}$$

where κ_i indicates the intrinsic thermal conductivity of the *i*-phase constituent [100–102]. Notice that the volume-averaged approach is only valid for the case where solid and fluid constituents are connected in parallel while computing the correct partial heat fluxes in Eq. (59) requires the geometric and topologic information of the pore structure obtained from 3D X-ray CT images [25,98,103–106]. Since the detailed geometrical attributes of the target porous media are not readily available, this extension will be considered in the future.

Let us now consider a small-scale problem $\nabla \cdot f(y) = 0$, while homogeneous energy balance requires $\nabla \cdot q^s = 0$ and $\nabla \cdot q^f = 0$ from Eqs. (30) and (33), respectively. Since f(y) can be additively decomposed into two parts, i.e., $f^s(y)$ and $f^f(y)$, the volume average of $\nabla \cdot f(y)$ can also be decomposed as,

$$\frac{1}{dV} \int_{\Omega} \nabla \cdot f(\mathbf{y}) \, d\Omega = \frac{1}{dV} \int_{\Omega} \nabla \cdot f^{s}(\mathbf{y}) \, d\Omega + \frac{1}{dV} \int_{\Omega} \nabla \cdot f^{f}(\mathbf{y}) \, d\Omega = 0. \tag{60}$$

Then, the averaging theorem [107] allows us to express the volume average of $\nabla \cdot f^i(y)$ $(i \in \{s, f\})$ as,

$$\frac{1}{dV} \int_{\Omega} \nabla \cdot f^{i}(\mathbf{y}) \, d\Omega = \underbrace{\nabla \cdot \left[\frac{1}{dV} \int_{\Omega} f^{i}(\mathbf{y}) \, d\Omega \right]}_{=\nabla \cdot \mathbf{q}^{i}} + \underbrace{\frac{1}{dV} \int_{\Gamma_{\Omega}} f^{i}(\mathbf{y}) \cdot \mathbf{n}_{i} \, d\Gamma}_{=-\mathbf{y}^{i}}, \tag{61}$$

where n_i is the outward unit normal vector from Ω_i , which satisfies $n_s = -n_f$, while Γ_{Ω} indicates the interface between the solid and fluid within a porous element Ω . Here, the second term on the right hand side of Eq. (61) is related to the rate of energy exchanges such that substituting both equations into the small scale problem in Eq. (61) yields the constraint $\chi^s + \chi^f = 0$ in Eq. (25). It underscores that the energy transfer between the constituents occurs at their interface Γ_{Ω} , implying that the macroscopic level description of heat exchange should be related to

the specific surface area of the material. Hence, this study adopts the model proposed by [49,107], which is based on Newton's law of cooling:

$$\chi^{s} = -\frac{1}{dV} \int_{\Gamma_{O}} \mathbf{f}^{s}(\mathbf{y}) \cdot \mathbf{n}_{s} d\Gamma = a_{m} h_{m}(\theta_{f} - \theta_{s}) \; ; \quad \chi^{f} = -\frac{1}{dV} \int_{\Gamma_{O}} \mathbf{f}^{f}(\mathbf{y}) \cdot \mathbf{n}_{f} d\Gamma = a_{m} h_{m}(\theta_{s} - \theta_{f}), \quad (62)$$

where a_m is the specific surface area of the porous matrix, and h_m is the interfacial heat transfer coefficient. Since we assumed that crack opening leads to complete fragmentation of solid skeleton, this study adopts the following relation for the specific surface area which assumes $a_m = a_{m,\text{max}}$ inside the fracture to replicate the case where fragmented solid particles are in suspension:

$$a_m = g(d)a_{m,ref} + [1 - g(d)]a_{m,max},$$
(63)

where $a_{m,ref}$ is the reference specific surface area of the material of interest, while we use $a_{m,max} = 3.0 \times 10^4$ m⁻¹ which is a typical value for coarse sands [108]. Although the interfacial heat transfer coefficient may not only depend on the pore space geometry but also the flow velocity, as we focus on low Reynolds number flow in both the bulk and crack regions, this study regards h_m as an independent material parameter for simplicity, following [83,89].

4.2. Hydromechanical responses in bulk and crack regions

At this point, we explicitly define the constitutive law that relates the fictitious undamaged effective stress σ'_0 and the strain measure ε , and also the temperature-dependent critical energy release rate \mathcal{G}_c . For porous medium with thermoelastic solid skeleton, the constitutive moduli can be defined as $\mathbb{C}^e = \lambda(I \otimes I) + \mu(\mathbb{I} + \overline{\mathbb{I}})$, where λ and μ are the Lamé constants, while undamaged effective stress in Eq. (18) becomes:

$$\sigma_0' = \lambda \operatorname{tr}(\boldsymbol{\varepsilon}) \boldsymbol{I} + 2\mu \boldsymbol{\varepsilon} - 3\alpha_s K(\theta_s - \theta_{s, ref}) \boldsymbol{I}. \tag{64}$$

As previous studies [12,109,110] have shown the relationship between fracture toughness and the temperature for rock, this study adopts the following constitutive model that can describe the θ_s -dependent \mathcal{G}_c , since we interpret cracking as the fracture of the solid skeleton [82]:

$$\mathcal{G}_c = \mathcal{G}_{c,\text{ref}} \left[1 - a_c \left(\frac{\theta_s - \theta_{s,\text{ref}}}{\theta_{s,\text{ref}}} \right) \right], \tag{65}$$

where $\mathcal{G}_{c,\text{ref}}$ is the critical energy release rate at the reference temperature $\theta_{s,\text{ref}}$, and $a_c > 0$ is the model parameter that accounts for temperature-dependent decrease of crack resistance.

In this study, the fluid flow within both undamaged porous matrix and fracture is assumed to be similar to the laminar flow of a Newtonian fluid that possesses a low Reynolds number. This approach has been widely accepted in modeling hydraulic fracture in porous media [78,111–114] such that the laminar fracture flow is approximated as the flow between two parallel plates which leads to an increase in permeability along the flow direction (i.e., cubic law). Hence, we assume that the fluid flow inside both the host matrix and the fracture obeys the generalized Darcy's law, i.e.,

$$\boldsymbol{w} = -\frac{\boldsymbol{k}}{\mu_f} (\nabla \ p_f - \rho_f \boldsymbol{g}), \tag{66}$$

where k is the permeability tensor and $\mu_f = \mu_f(\theta_f)$ is the dynamic viscosity of the pore fluid. Here, the permeability tensor can be idealized as the summation of the isotropic matrix permeability and the part that accounts for the anisotropic enhancement due to the crack opening [41,78,79,112]:

$$\mathbf{k} = \mathbf{k}_{\text{mat}} + \mathbf{k}^c = k_{\text{mat}} \mathbf{I} + d^2 k_c (\mathbf{I} - \mathbf{n}_c \otimes \mathbf{n}_c), \tag{67}$$

where k_{mat} is the effective permeability of the undamaged porous matrix, $\mathbf{n}_c = \nabla d/\|\nabla d\|$ is the unit normal of crack surface, and k_c is the permeability enhancement due to the crack opening and it depends on the fracture aperture w_c :

$$k_c = \frac{w_c^2}{12} \; ; \; w_c = H(d) \left[l_f (1 + \mathbf{n}_c \cdot \boldsymbol{\varepsilon} \cdot \mathbf{n}_c) \right] \; ; \; H(d) = \begin{cases} 0 & \text{if } d \le 0.5, \\ 1 & \text{if } d > 0.5, \end{cases}$$
 (68)

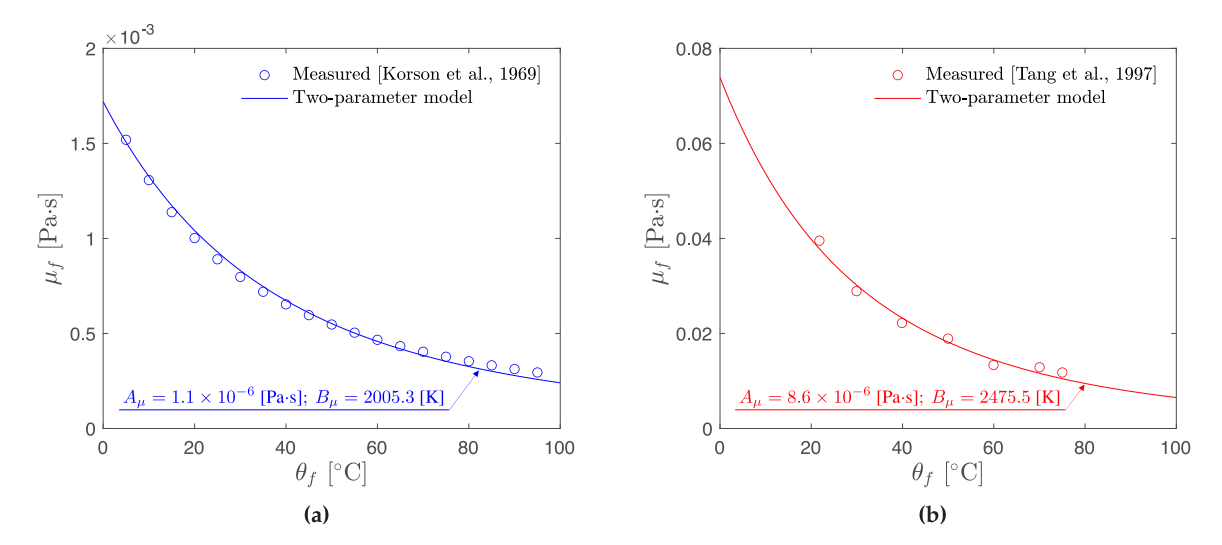


Fig. 2. Temperature-dependent viscosity of (a) pure water, and (b) A-95 crude oil.

with l_f denoting the characteristic length that has been assumed to be equal to the finite element size (i.e., $l_f = h_e$) [45,78,111], while H(d) is the Heaviside function that explicitly defines the fractured zone based on the assumption that fracture flow is initiated if the material is half-damaged [80]. By revisiting Eq. (14), notice that semi-empirical porosity-permeability relation may not be applicable in this study since $\phi^f = 1$ if the host matrix is completely damaged. In this case, precise prediction of matrix permeability may require other geometrical features such as formation factor, tortuosity, or shape of pores [105,115–118]. This extension is out of the scope of this study, and hence, we consider k_{mat} as a constant.

As the viscosity of many fluids are temperature-dependent, numerical results drawn from the fluid flow with constant viscosity are often not applicable in the non-isothermal state [119–121]. Specifically, the temperature dependence of pore fluid viscosity affects the diffusion coefficient in Eq. (66) which may lead to different flow patterns compared to the idealized case where viscosity is assumed to be a constant. In this study, we adopt the most popular empirical formula that consists of two parameters (A_{μ} and B_{μ}) as follows [122,123]:

$$\mu_f = A_\mu \exp(B_\mu \theta_f^{-1}).$$
 (69)

Even though there is no one formula that works for all fluids, the two-parameter exponential model is capable of predicting the temperature-dependent viscosity of water and crude oil as shown in Fig. 2, which are the two most common types of pore fluids in geomaterials. Note that the circular symbols in Figs. 2(a) and 2(b) denote experimentally measured data for water [124] and A-95 crude oil [125], respectively, while solid curves indicate the curve-fitted results from Eq. (69).

5. Asynchronous time integration scheme

This section focuses on the solution strategy for the coupled problem, while the detailed procedure to obtain its semi-discrete form is summarized in Appendix. We introduce a special time integration scheme that adopts different time step sizes for the solid and fluid temperatures by using the concept of isothermal operator split and subcycling method [87,126,127]. Compared to two other solution strategies (i.e., monolithic and isothermal split solvers with a single time step), numerical analysis in Section 6.1 hints that our approach yields consistent results while being computationally more efficient. We also conduct a stability analysis for the multi-time-step integration through investigating the generalized eigenvalue problem, while we suggest the optimal time step size and cycling period for the implicit time integration scheme by adopting more restrictive conditions: the discrete maximum and the monotonicity principles [128–131].

5.1. Operator splitting and multi-time-step integration

By letting \mathbf{u} , \mathbf{p} , \mathbf{T}_s , \mathbf{T}_f , and \mathbf{d} be the nodal vectors for the displacement, pore pressure, solid temperature, fluid temperature, and phase field, respectively, we directly start from the semi-discrete form of the governing field equations [Eqs. (30), (33), (44), (45), and (55)] for brevity:

$$\mathbf{K}\mathbf{u} - \mathbf{G}\mathbf{p} - \mathbf{P}\mathbf{T}_{s} = \mathbf{f}_{u},\tag{70}$$

$$\mathbf{G}^{\mathrm{T}}\dot{\mathbf{u}} + \mathbf{C}\dot{\mathbf{p}} - \mathbf{H}\dot{\mathbf{T}}_{\mathrm{s}} + \mathbf{\Phi}\mathbf{p} = \mathbf{f}_{\mathrm{p}},\tag{71}$$

$$\mathbf{S}_{s}\dot{\mathbf{T}}_{s} + (\mathbf{O}_{s} + \mathbf{E}_{s})\mathbf{T}_{s} - \mathbf{D}\mathbf{T}_{f} = \mathbf{f}_{s},\tag{72}$$

$$\mathbf{S}_{\mathbf{f}}\dot{\mathbf{T}}_{\mathbf{f}} - \mathbf{D}^{\mathsf{T}}\mathbf{T}_{\mathbf{s}} + (\mathbf{A} + \mathbf{Q}_{\mathbf{f}} + \mathbf{E}_{\mathbf{f}})\mathbf{T}_{\mathbf{f}} = \mathbf{f}_{\mathbf{f}},\tag{73}$$

$$\mathbf{\Lambda d} = \mathbf{f}_{d},\tag{74}$$

while the complete procedure including detailed expressions for all the vectors and matrices are summarized in Appendix. In this study, we adopt the staggered scheme that updates the phase field \mathbf{d} and all other variables $\{\mathbf{u}, \mathbf{p}, \mathbf{T}_s, \mathbf{T}_f\}$ separately, which may potentially be more robust compared to the solution scheme that simultaneously solves the complete system of equations [i.e., Eqs. (70)–(74)] with a single solver [42,44,69,132,133]. Thus, by regarding the staggered scheme for the phase field \mathbf{d} as a default setting, we will use the term *monolithic* to indicate the scenario where we use a single solver to solve Eqs. (70)–(73), while the term *operator split* will indicate the scenario where the field variables \mathbf{u} , \mathbf{p} , \mathbf{T}_s , and \mathbf{T}_f are updated separately even if they are advanced in a staggered manner.

To solve the semi-discrete form of the governing equations numerically, it is required to choose a time-stepping integrator that leads to a different structure of the algebraic problem [27,87,134–136]. Although one may choose different strategies to solve the same system, this study focuses on three different time integration methods as shown in Fig. 3. The first method, i.e., case (a), is often referred to as monolithic or simultaneous solution scheme and can be obtained by adopting a single time integrator which updates $\{\mathbf{u}, \mathbf{p}, \mathbf{T}_s, \mathbf{T}_f\}$ simultaneously, while the second case (b) adopts a time integration scheme that requires decoupling of the semi-discrete field equations into two parts: isothermal poromechanics problem that solves $\{\mathbf{u}, \mathbf{p}\}$ and heat transfer problem that advances $\{\mathbf{T}_s, \mathbf{T}_f\}$. This strategy is often referred to as an isothermal operator split [87,135,137]. Our new contribution here is to develop a third strategy (c) that uses different time steps for solid and fluid constituents that are thermally non-equilibrated. Similar to the subcycling method [126,127,138,139], this approach eliminates the need to update the entire set of variables $\{\mathbf{T}_s, \mathbf{T}_f\}$ with a single time step, while it allows us to adopt different time step sizes for \mathbf{T}_s and \mathbf{T}_f that may be computationally more efficient compared to the cases (a) and (b).

The first method (a) shown in Fig. 3 is the simplest approach that monolithically solves the following block-partitioned system:

$$\begin{bmatrix}
0 & 0 & 0 & 0 \\
G^{T} & C & -H & 0 \\
0 & 0 & S_{s} & 0 \\
0 & 0 & 0 & S_{f}
\end{bmatrix}
\underbrace{\begin{bmatrix}
\dot{\mathbf{u}} \\
\dot{\mathbf{p}} \\
\dot{\mathbf{T}}_{s} \\
\dot{\mathbf{T}}_{f}
\end{bmatrix}}_{=\dot{\mathbf{M}}_{mono}} + \underbrace{\begin{bmatrix}
\mathbf{K} & -G & -P & 0 \\
0 & \Phi & 0 & 0 \\
0 & 0 & Q_{s} + E_{s} & -D \\
0 & 0 & -D^{T} & \mathbf{A} + Q_{f} + E_{f}
\end{bmatrix}}_{=\dot{\mathbf{K}}_{mono}} \underbrace{\begin{bmatrix}
\mathbf{u} \\
\mathbf{p} \\
T_{s} \\
T_{f}
\end{bmatrix}}_{=\mathbf{x}_{mono}} = \underbrace{\begin{bmatrix}
\mathbf{f}_{u} \\
\mathbf{f}_{p} \\
\mathbf{f}_{s} \\
\mathbf{f}_{f}
\end{bmatrix}}_{=\mathbf{x}_{mono}}, \tag{75}$$

with the following stabilization parameter [140–142]:

$$\tau_{\text{SUPG}} = \left[\left(\frac{2}{\Delta t} \right)^2 + \left(\frac{2 \| \boldsymbol{w} \|}{\rho_f c_f h_e} \right)^2 + 9 \left(\frac{4 \phi^f \kappa_f}{\rho_f c_f h_e^2} \right)^2 \right]^{-1/2}.$$
 (76)

From Eq. (75), the generalized trapezoidal rule [e.g., $\mathbf{x}_{mono}^{n+1} = \mathbf{x}_{mono}^n + (1-\beta)\Delta t\dot{\mathbf{x}}_{mono}^n + \beta\Delta t\dot{\mathbf{x}}_{mono}^{n+1}$] yields the following system that needs to be solved:

(a)
$$(\bar{\mathbf{M}}_{\text{mono}} + \beta \Delta t \bar{\mathbf{K}}_{\text{mono}}) \mathbf{x}_{\text{mono}}^{n+1} = [\bar{\mathbf{M}}_{\text{mono}} + (1 - \beta) \Delta t \bar{\mathbf{K}}_{\text{mono}}] \mathbf{x}_{\text{mono}}^{n} + \Delta t [(1 - \beta) \bar{\mathbf{f}}_{\text{mono}}^{n} + \beta \bar{\mathbf{f}}_{\text{mono}}^{n+1}],$$
 (77)

where $\mathbf{x}_{\text{mono}}^{\text{n}} = \mathbf{x}_{\text{mono}}(t^{\text{n}}) = \mathbf{x}_{\text{mono}}(n\Delta t)$, and the parameter β determines the integration algorithm, e.g., $\beta = 0$ yields a forward Euler and $\beta = 1$ recovers a backward Euler method. Note that the integration is implicit without any restriction on Δt if $\beta \geq 1/2$.

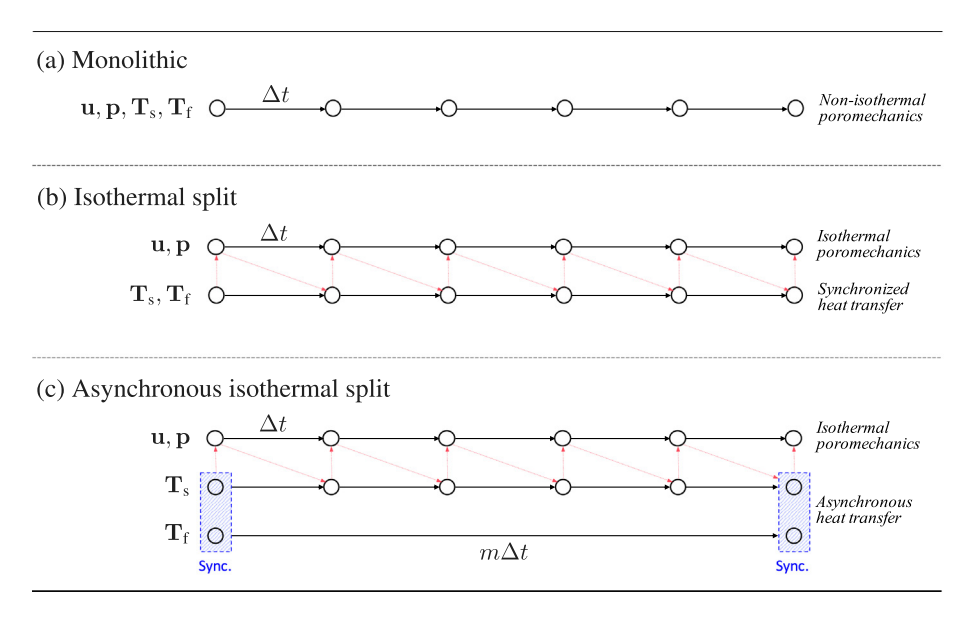


Fig. 3. Time integration schemes: (a) monolithic, (b) isothermal split, and (c) asynchronous isothermal split.

On the other hand, the isothermal operator split used for the cases (b) and (c) requires the following block-partitioned systems that are decoupled:

$$\underbrace{\begin{bmatrix} \mathbf{0} & \mathbf{0} \\ \mathbf{G}^{\mathrm{T}} & \mathbf{C} \end{bmatrix}}_{=\tilde{\mathbf{M}}_{\mathrm{up}}} \underbrace{\begin{bmatrix} \dot{\mathbf{u}} \\ \dot{\mathbf{p}} \end{bmatrix}}_{=\tilde{\mathbf{x}}_{\mathrm{up}}} + \underbrace{\begin{bmatrix} \mathbf{K} & -\mathbf{G} \\ \mathbf{0} & \boldsymbol{\Phi} \end{bmatrix}}_{=\tilde{\mathbf{K}}_{\mathrm{up}}} \underbrace{\begin{bmatrix} \mathbf{u} \\ \mathbf{p} \end{bmatrix}}_{=\mathbf{x}_{\mathrm{up}}} = \underbrace{\begin{bmatrix} \mathbf{f}_{\mathrm{u}} + \mathbf{P}\hat{\mathbf{T}}_{\mathrm{s}} \\ \mathbf{f}_{\mathrm{p}} + \mathbf{H}\hat{\mathbf{T}}_{\mathrm{s}} \end{bmatrix}}_{=\tilde{\mathbf{f}}_{\mathrm{up}}}, \tag{78}$$

$$\underbrace{\begin{bmatrix} \mathbf{S}_{s} & \mathbf{0} \\ \mathbf{0} & \mathbf{S}_{f} \end{bmatrix}}_{=\tilde{\mathbf{X}}_{sf}} \underbrace{\begin{bmatrix} \dot{\mathbf{T}}_{s} \\ \dot{\mathbf{T}}_{f} \end{bmatrix}}_{=\tilde{\mathbf{X}}_{sf}} + \underbrace{\begin{bmatrix} \mathbf{Q}_{s} + \mathbf{E}_{s} & -\mathbf{D} \\ -\mathbf{D}^{T} & \mathbf{A} + \mathbf{Q}_{f} + \mathbf{E}_{f} \end{bmatrix}}_{=\tilde{\mathbf{K}}_{sf}} \underbrace{\begin{bmatrix} \mathbf{T}_{s} \\ \mathbf{T}_{f} \end{bmatrix}}_{=\tilde{\mathbf{X}}_{sf}} = \underbrace{\begin{bmatrix} \mathbf{f}_{s} \\ \mathbf{f}_{f} \end{bmatrix}}_{=\tilde{\mathbf{X}}_{sf}}, \tag{79}$$

Here, the superimposed hat in Eq. (78) indicates that corresponding nodal vectors are readily determined since isothermal splitting solution scheme implies that \mathbf{T}_s and \mathbf{T}_f are no longer unknown variables for the poromechanics problem under isothermal condition [87,143–145].

For case (b) illustrated in Fig. 3, the isothermal poromechanics problem and the heat transfer problem share the same Δt . Specifically, as indicated with red dashed lines with arrows in Fig. 3, omitting the Gauss–Seidel iteration, $\hat{\mathbf{T}}_s$ and $\hat{\mathbf{T}}_s$ in Eq. (78) are updated from Eq. (79) (i.e., $\hat{\mathbf{T}}_s = \mathbf{T}_s^{n+1}$ and $\hat{\mathbf{T}}_s = \dot{\mathbf{T}}_s^{n+1}$). In this case, the stabilization parameter τ_{SUPG} remains unchanged compared to case (a), while the generalized trapezoidal rule yields the following system:

(b)
$$\begin{cases} (\bar{\mathbf{M}}_{up} + \beta_{up} \Delta t \bar{\mathbf{K}}_{up}) \mathbf{x}_{up}^{n+1} = \left[\bar{\mathbf{M}}_{up} + (1 - \beta_{up}) \Delta t \bar{\mathbf{K}}_{up} \right] \mathbf{x}_{up}^{n} + \Delta t \left[(1 - \beta_{up}) \bar{\mathbf{f}}_{up}^{n} + \beta_{up} \bar{\mathbf{f}}_{up}^{n+1} \right], & \text{(a)} \\ (\bar{\mathbf{M}}_{sf} + \beta_{sf} \Delta t \bar{\mathbf{K}}_{sf}) \mathbf{x}_{sf}^{n+1} = \left[\bar{\mathbf{M}}_{sf} + (1 - \beta_{sf}) \Delta t \bar{\mathbf{K}}_{sf} \right] \mathbf{x}_{sf}^{n} + \Delta t \left[(1 - \beta_{sf}) \bar{\mathbf{f}}_{sf}^{n} + \beta_{sf} \bar{\mathbf{f}}_{sf}^{n+1} \right], & \text{(b)} \end{cases}$$

where the parameters β_{up} and β_{sf} indicate that the isothermal operator splitting in case (b) requires two distinct time integrators.

For case (c) where we adopt the mixed time integration for the heat transfer problem (i.e., asynchronous heat transfer), we assume that the nodal groups \mathbf{T}_s and \mathbf{T}_f in a column vector \mathbf{x}_{sf} are integrated with different time steps Δt and $m\Delta t$, respectively (Fig. 3), where $m \geq 1$ is an integer. Here, time step $m\Delta t$ is called cycle [126,146] that corresponds to the synchronized step in this study where both \mathbf{T}_s and \mathbf{T}_f are updated simultaneously. The integration cycle for \mathbf{x}_{sf} can be defined by re-writing the generalized trapezoidal rule as,

$$\mathbf{x}_{sf}^{n+1} = \mathbf{x}_{sf}^{n} + \Delta t \mathbf{W}_{1} \dot{\mathbf{x}}_{sf}^{n} + \Delta t \mathbf{W}_{2} \dot{\mathbf{x}}_{sf}^{n+1}, \tag{81}$$

with,

$$\mathbf{W}_{1} = \begin{cases} \begin{bmatrix} (1 - \beta_{sf})\mathbf{I} & \mathbf{0} \\ \mathbf{0} & \mathbf{0} \end{bmatrix} & \text{if } 1 \leq n \leq m - 1, \\ \begin{bmatrix} (1 - \beta_{sf})\mathbf{I} & \mathbf{0} \\ \mathbf{0} & m(1 - \beta_{sf})\mathbf{I} \end{bmatrix} & \text{if } n = m, \end{cases} ; \quad \mathbf{W}_{2} = \begin{cases} \begin{bmatrix} \beta_{sf}\mathbf{I} & \mathbf{0} \\ \mathbf{0} & \mathbf{0} \end{bmatrix} & \text{if } 1 \leq n \leq m - 1, \\ \begin{bmatrix} \beta_{sf}\mathbf{I} & \mathbf{0} \\ \mathbf{0} & m\beta_{sf}\mathbf{I} \end{bmatrix} & \text{if } n = m, \end{cases}$$

$$(82)$$

where **I** is the unit matrix that is different from the identity tensor **I**. Substituting Eq. (81) into Eq. (79) yields the following set of equations that needs to be solved, while we assume that the solution for the isothermal poromechanics problem is advanced by Δt , such that the system in Eq. (83)(a) remains the same compared to Eq. (80)(a), i.e.,

(c)
$$\begin{cases} (\bar{\mathbf{M}}_{up} + \beta_{up} \Delta t \bar{\mathbf{K}}_{up}) \mathbf{x}_{up}^{n+1} = \left[\bar{\mathbf{M}}_{up} + (1 - \beta_{up}) \Delta t \bar{\mathbf{K}}_{up} \right] \mathbf{x}_{up}^{n} + \Delta t \left[(1 - \beta_{up}) \bar{\mathbf{f}}_{up}^{n} + \beta_{up} \bar{\mathbf{f}}_{up}^{n+1} \right], & \text{(a)} \\ (\bar{\mathbf{M}}_{sf} + \Delta t \mathbf{W}_{2} \bar{\mathbf{K}}_{sf}) \mathbf{x}_{sf}^{n+1} = (\bar{\mathbf{M}}_{sf} - \Delta t \mathbf{W}_{1} \bar{\mathbf{K}}_{sf}) \mathbf{x}_{sf}^{n} + \Delta t (\mathbf{W}_{1} \bar{\mathbf{f}}_{sf}^{n} + \mathbf{W}_{2} \bar{\mathbf{f}}_{sf}^{n+1}), & \text{(b)} \end{cases}$$

while the stabilization parameter is redefined accordingly for this case

$$\tau_{\text{SUPG}} = \left[\left(\frac{2}{m\Delta t} \right)^2 + \left(\frac{2\|\mathbf{w}\|}{\rho_f c_f h_e} \right)^2 + 9 \left(\frac{4\phi^f \kappa_f}{\rho_f c_f h_e^2} \right)^2 \right]^{-1/2}. \tag{84}$$

Note that Eq. (83)(a) and (83)(b) summarize the solution scheme in a single cycle for case (c), while the entire code structure for the mixed time integration is illustrated in Fig. 4, where the gray blocks denote the initialization steps, the red blocks represent time-marching procedure, and blue blocks indicate the Gauss–Seidel iteration. Here, if we set the maximum number of iterations to be 1, the Gauss–Seidel iteration reduces to a series of staggered solution schemes.

5.2. Stability of mixed time integration

As previous studies [137,147,148] have investigated the stability and convergence for the hydro-mechanically coupled problem, we focus on the stability analysis on the mixed time integration in Eq. (83)(b) since it reduces to a standard isothermal split setting for case (b) shown in Fig. 3 if m = 1. In specific, this section focuses on the case where the stabilization parameter τ_{SUPG} is small, so that the matrices \mathbf{S}_f , \mathbf{A} , and \mathbf{Q}_f are considered symmetric. Considering the homogeneous case, Eq. (83)(b) reduces into,

$$(\underline{\bar{\mathbf{M}}_{sf} + \Delta t \mathbf{W}_{2} \bar{\mathbf{K}}_{sf}}) \mathbf{x}_{sf}^{n+1} = (\underline{\bar{\mathbf{M}}_{sf} - \Delta t \mathbf{W}_{1} \bar{\mathbf{K}}_{sf}}) \mathbf{x}_{sf}^{n},$$

$$= \underline{\bar{\mathbf{A}}_{1}}$$
(85)

which leads to the following generalized eigenvalue problem that is essential to investigate the stability characteristics:

$$\bar{\mathbf{A}}_{1}\mathbf{y}_{sf} = \lambda_{sf}\bar{\mathbf{A}}_{2}\mathbf{y}_{sf} \; ; \; \mathbf{y}_{sf} = \begin{bmatrix} \mathbf{y}_{s} \\ \mathbf{y}_{f} \end{bmatrix}, \tag{86}$$

where the vector \mathbf{y}_{sf} is composed of total $N_n^{sf} = N_n^s + N_n^f$ components so that its ith element corresponds to \mathbf{y}_s that is related to the solid temperature, if $1 \le i \le N_n^s$; while corresponds to \mathbf{y}_f (i.e., the fluid temperature) if $N_n^s + 1 \le i \le N_n^{sf}$.

For the non-synchronized step where $1 \le n \le m-1$, we get the following by substituting Eq. (82) into Eq. (86):

$$\begin{bmatrix} \mathbf{Q}_{s} + \mathbf{E}_{s} & -\mathbf{D} \\ \mathbf{0} & \mathbf{0} \end{bmatrix} \mathbf{y}_{sf} = \underbrace{\frac{1 - \lambda_{sf}}{(1 - \beta_{sf})\Delta t + \lambda_{sf}\beta_{sf}\Delta t}}_{=\mathbf{V}_{s}} \mathbf{\bar{M}}_{sf}\mathbf{y}_{sf} \longrightarrow \begin{cases} (\mathbf{Q}_{s} + \mathbf{E}_{s})\mathbf{y}_{s} - \mathbf{D}\mathbf{y}_{f} = \gamma_{sf}\mathbf{S}_{s}\mathbf{y}_{s}, \\ \mathbf{0} = \gamma_{sf}\mathbf{S}_{f}\mathbf{y}_{f}. \end{cases}$$
(87)

Following Smolinski et al. [126], due to the positive definiteness of S_s , the second row in Eq. (87) implies either $\gamma_{sf} = 0$ or $y_f = 0$. In specific, if $1 \le i \le N_n^s$, we have $\gamma_{sf} = 0$; while $y_f = 0$ for $N_n^s + 1 \le i \le N_n^{sf}$. Considering the

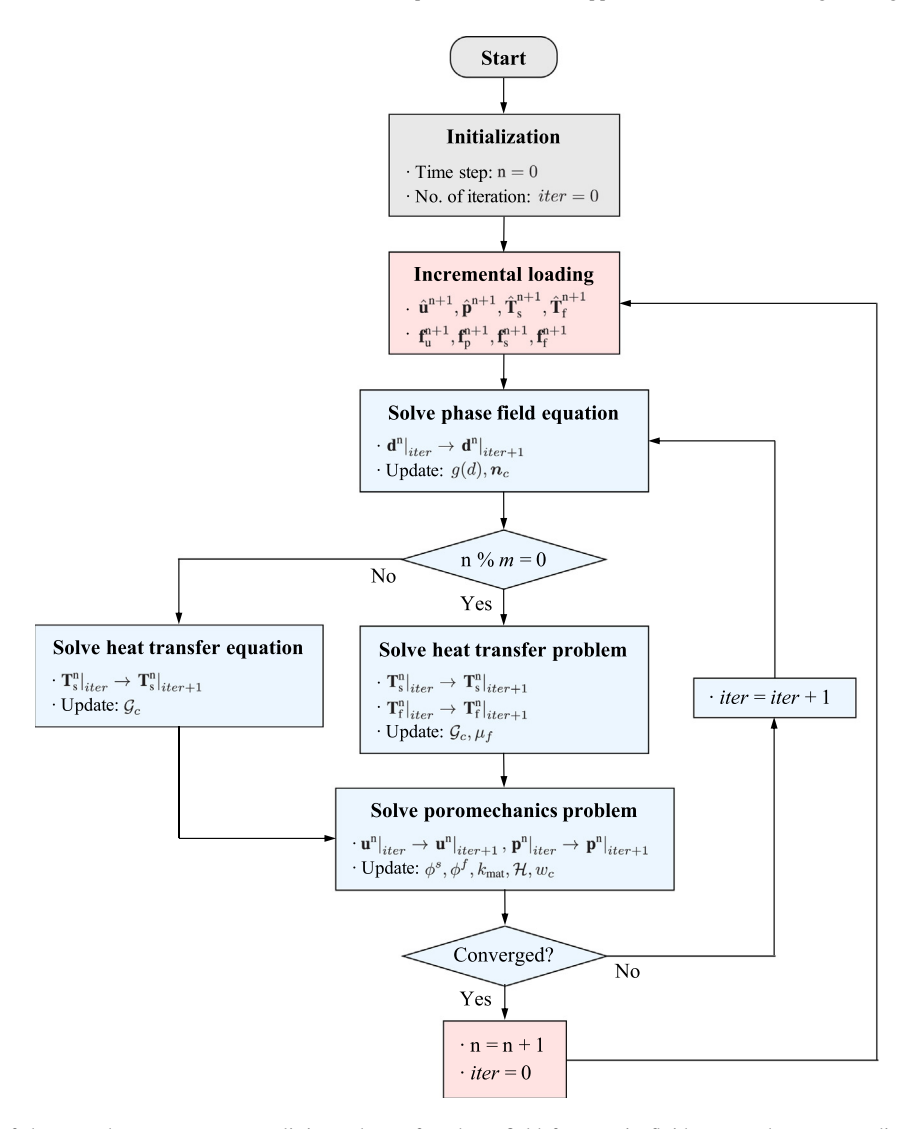


Fig. 4. Flowchart of the asynchronous operator splitting scheme for phase field fracture in fluid-saturated porous media under local thermal non-equilibrium.

first case where $\gamma_{sf} = 0$, the first row in Eq. (87) yields $\mathbf{y}_s = \left[(\mathbf{Q}_s + \mathbf{E}_s)^{-1} \mathbf{D} \right] \mathbf{y}_f$, such that the vector \mathbf{y}_{sf} spans $\mathbb{R}^{N_n^f}$ since $\mathbf{Q}_s + \mathbf{E}_s$ is a symmetric and non-singular matrix, i.e.,

$$\tilde{\mathbf{y}}_{sf} = \begin{bmatrix} [(\mathbf{Q}_s + \mathbf{E}_s)^{-1} \mathbf{D}] \tilde{\mathbf{y}}_f \\ \tilde{\mathbf{y}}_f \end{bmatrix} \quad \text{if } 1 \le i \le N_n^s, \tag{88}$$

where the superposed tilde indicates the prospective eigenvectors that correspond to $\gamma_{sf} = 0$. On the other hand, for the second case where $\mathbf{y}_f = \mathbf{0}$, vector \mathbf{y}_{sf} spans $\mathbb{R}^{N_n^s}$ and is given by,

$$\check{\mathbf{y}}_{\mathrm{sf}} = \begin{bmatrix} \check{\mathbf{y}}_{\mathrm{s}} \\ \mathbf{0} \end{bmatrix} \quad \text{if } N_n^{\mathrm{s}} + 1 \le i \le N_n^{\mathrm{sf}}. \tag{89}$$

Here, the superposed check symbol in Eq. (89) denotes the prospective eigenvectors that correspond to the case where $\mathbf{y}_f = \mathbf{0}$. Notice that Eqs. (88) and (89) hint that the set of vectors ($\tilde{\mathbf{y}}_{sf}$ and $\check{\mathbf{y}}_{sf}$) span $\mathbb{R}^{N_n^{sf}}$. It implies that we have two sets of eigenvectors that correspond to the case where the eigenvalues are either $\gamma_{sf} = 0$ or $\gamma_{sf} \neq 0$, respectively, since they are orthogonal with respect to $\bar{\mathbf{K}}_{sf}$. Specifically, the vectors $\check{\mathbf{y}}_{sf}$ are B-orthogonal to each

other [149–151]:

$$\check{\mathbf{y}}_{\mathrm{sf},i}^{\mathrm{T}}\bar{\mathbf{K}}_{\mathrm{sf}}\check{\mathbf{y}}_{\mathrm{sf},j} = \begin{bmatrix} \check{\mathbf{y}}_{\mathrm{s},i}^{\mathrm{T}} & \mathbf{0}^{\mathrm{T}} \end{bmatrix} \begin{bmatrix} \mathbf{Q}_{\mathrm{s}} + \mathbf{E}_{\mathrm{s}} & -\mathbf{D} \\ -\mathbf{D}^{\mathrm{T}} & \mathbf{A} + \mathbf{Q}_{\mathrm{f}} + \mathbf{E}_{\mathrm{f}} \end{bmatrix} \begin{bmatrix} \check{\mathbf{y}}_{\mathrm{s},j} \\ \mathbf{0} \end{bmatrix}
= \begin{bmatrix} \check{\mathbf{y}}_{\mathrm{s},i}^{\mathrm{T}} & \mathbf{0}^{\mathrm{T}} \end{bmatrix} \begin{bmatrix} (\mathbf{Q}_{\mathrm{s}} + \mathbf{E}_{\mathrm{s}})\check{\mathbf{y}}_{\mathrm{s},j} \\ -\mathbf{D}^{\mathrm{T}}\check{\mathbf{y}}_{\mathrm{s},j} \end{bmatrix} = \check{\mathbf{y}}_{\mathrm{s},i}^{\mathrm{T}} (\mathbf{Q}_{\mathrm{s}} + \mathbf{E}_{\mathrm{s}})\check{\mathbf{y}}_{\mathrm{s},j} = \gamma_{\mathrm{sf},i}\delta_{ij} \quad \text{if } \{i,j\} \in [1,N_n^{\mathrm{s}}], \tag{90}$$

since the first row in Eq. (87) gives $(\mathbf{Q}_s + \mathbf{E}_s)\check{\mathbf{y}}_s = \gamma_{sf}\mathbf{S}_s\check{\mathbf{y}}_s$, such that $\check{\mathbf{y}}_s$ can be orthogonalized with respect to $\mathbf{Q}_s + \mathbf{E}_s$ and \mathbf{S}_s , whereas the vectors $\check{\mathbf{y}}_{sf}$ are orthogonal to $\check{\mathbf{y}}_{sf}$ with respect to $\bar{\mathbf{K}}_{sf}$:

$$\check{\mathbf{y}}_{\mathrm{sf},i}^{\mathrm{T}}\bar{\mathbf{K}}_{\mathrm{sf}}\tilde{\mathbf{y}}_{\mathrm{sf},j} = \begin{bmatrix} \check{\mathbf{y}}_{\mathrm{s},i}^{\mathrm{T}} & \mathbf{0}^{\mathrm{T}} \end{bmatrix} \begin{bmatrix} \mathbf{Q}_{\mathrm{s}} + \mathbf{E}_{\mathrm{s}} & -\mathbf{D} \\ -\mathbf{D}^{\mathrm{T}} & \mathbf{A} + \mathbf{Q}_{\mathrm{f}} + \mathbf{E}_{\mathrm{f}} \end{bmatrix} \begin{bmatrix} [(\mathbf{Q}_{\mathrm{s}} + \mathbf{E}_{\mathrm{s}})^{-1}\mathbf{D}] \, \tilde{\mathbf{y}}_{\mathrm{f},j} \\ \tilde{\mathbf{y}}_{\mathrm{f},j} \end{bmatrix} \\
= \begin{bmatrix} \check{\mathbf{y}}_{\mathrm{s},i}^{\mathrm{T}} & \mathbf{0}^{\mathrm{T}} \end{bmatrix} \begin{bmatrix} -\mathbf{D}^{\mathrm{T}}(\mathbf{Q}_{\mathrm{s}} + \mathbf{E}_{\mathrm{s}})\mathbf{D} + (\mathbf{A} + \mathbf{Q}_{\mathrm{f}} + \mathbf{E}_{\mathrm{f}}) \tilde{\mathbf{y}}_{\mathrm{f},j} \end{bmatrix} = 0 \quad \text{if } \{i, j\} \in [N_{n}^{\mathrm{s}} + 1, N_{n}^{\mathrm{sf}}]. \tag{91}$$

Therefore, the non-synchronized solution at time step n can be expanded in terms of eigenvectors as,

$$\mathbf{x}_{sf}^{n} = \check{c}_{i}\check{\mathbf{y}}_{sf,i} + \tilde{c}_{i}\check{\mathbf{y}}_{sf,i}, \tag{92}$$

where \check{c}_i and \tilde{c}_j are constants, while the repeated indices imply the summation following the Einstein's notation [86, 152]. Then, substituting Eq. (92) into Eq. (85) yields the following expression for the updated solution:

$$\mathbf{x}_{sf}^{n+1} = \check{c}_i \lambda_{sf,i} \check{\mathbf{y}}_{sf,i} + \tilde{c}_i \tilde{\mathbf{y}}_{sf,j}, \tag{93}$$

where $\lambda_{sf} = 1$ for $\tilde{\mathbf{y}}_{sf}$ since $\gamma_{sf} = 0$. By defining the norm E_{sf} as,

$$E_{\rm sf} = \frac{1}{2} \mathbf{x}_{\rm sf}^{\rm T} \bar{\mathbf{K}}_{\rm sf} \mathbf{x}_{\rm sf},\tag{94}$$

the B-orthogonality shown in Eqs. (90) and (91) gives the following expression for time step n:

$$E_{\rm sf}^{\rm n} = (\check{c}_l \check{\mathbf{y}}_{{\rm sf},i} + \tilde{c}_j \widetilde{\mathbf{y}}_{{\rm sf},j})^{\rm T} \bar{\mathbf{K}}_{\rm sf} (\check{c}_k \check{\mathbf{y}}_{{\rm sf},k} + \tilde{c}_l \widetilde{\mathbf{y}}_{{\rm sf},l}) = \check{c}_i^2 \gamma_{{\rm sf},i} + \tilde{c}_j \tilde{c}_l \check{\mathbf{y}}_{{\rm sf},j}^{\rm T} \bar{\mathbf{K}}_{{\rm sf}} \check{\mathbf{y}}_{{\rm sf},l}, \tag{95}$$

while $E_{\rm sf}^{\rm n+1}$ at time step n + 1 reads,

$$E_{\rm sf}^{\rm n+1} = (\check{c}_i \lambda_{{\rm sf},i} \check{\mathbf{y}}_{{\rm sf},i} + \tilde{c}_j \tilde{\mathbf{y}}_{{\rm sf},j})^{\rm T} \bar{\mathbf{K}}_{\rm sf} (\check{c}_k \lambda_{{\rm sf},k} \check{\mathbf{y}}_{{\rm sf},k} + \tilde{c}_l \tilde{\mathbf{y}}_{{\rm sf},l}) = \check{c}_i^2 \lambda_{{\rm sf},i}^2 \gamma_{{\rm sf},i} + \tilde{c}_j \tilde{c}_l \tilde{\mathbf{y}}_{{\rm sf},j}^{\rm T} \bar{\mathbf{K}}_{{\rm sf}} \tilde{\mathbf{y}}_{{\rm sf},l}. \tag{96}$$

Comparing Eqs. (95) and (96), notice that the stability $E_{\rm sf}^{\rm n+1} \leq E_{\rm sf}^{\rm n}$ is ensured if the following condition is satisfied:

$$|\lambda_{\rm sf}| = \left| \frac{1 - \gamma_{\rm sf} (1 - \beta_{\rm sf}) \Delta t}{1 + \gamma_{\rm sf} \beta_{\rm sf} \Delta t} \right| \le 1. \tag{97}$$

If $\gamma_{\rm sf} \ge 0$, Eq. (97) reduces into,

$$\Delta t \le \frac{2}{\nu_{\rm sf}(1 - 2\beta_{\rm sf})}.\tag{98}$$

For the synchronized step where n=m, Eqs. (85) and (86) yield the following expression with some rearrangements:

$$\bar{\mathbf{K}}_{\mathrm{sf}}\mathbf{y}_{\mathrm{sf}} = \underbrace{\frac{1 - \lambda_{\mathrm{sf}}'}{m\left[(1 - \beta_{\mathrm{sf}})\Delta t + \lambda_{\mathrm{sf}}'\beta_{\mathrm{sf}}\Delta t\right]}}_{=\gamma_{\mathrm{sf}}'} \underbrace{\begin{bmatrix} m\mathbf{S}_{\mathrm{s}} & \mathbf{0} \\ \mathbf{0} & \mathbf{S}_{\mathrm{f}} \end{bmatrix}}_{=\bar{\mathbf{M}}_{\mathrm{sf}}'} \mathbf{y}_{\mathrm{sf}},\tag{99}$$

where λ'_{sf} , γ'_{sf} and $\bar{\mathbf{M}}'_{sf}$ designate the quantities associated with the synchronized step. Here, since $\bar{\mathbf{K}}_{sf}$ and $\bar{\mathbf{M}}'_{sf}$ are symmetric and non-singular based on the assumption $\tau_{SUPG} \to 0$, the values γ'_{sf} are real and possess distinct eigenvectors \mathbf{y}_{sf} that are B-orthogonal [149–151]. Thus, following the similar procedure that is used for the non-synchronized step [i.e., Eqs. (94)–(97)], the stability condition reads,

$$|\lambda_{\rm sf}'| = \left| \frac{1 - m\gamma_{\rm sf}'(1 - \beta_{\rm sf})\Delta t}{1 + m\gamma_{\rm sf}'\beta_{\rm sf}\Delta t} \right| \le 1. \tag{100}$$

Similarly, if $\gamma'_{sf} \ge 0$, Eq. (100) reduces into,

$$\Delta t \le \frac{2}{m\gamma_{\rm sf}'(1 - 2\beta_{\rm sf})}.\tag{101}$$

This stability analysis highlights that our mixed time integration is unconditionally stable if we adopt implicit schemes. For example, if we employ the backward Euler method (i.e., $\beta_{sf} = 1$), the stability conditions are automatically satisfied since both $|\lambda_{sf}|$ and $|\lambda_{sf}'|$ are less than 1, i.e.,

$$|\lambda_{\rm sf}| = \left| \frac{1}{1 + \gamma_{\rm sf} \Delta t} \right| < 1 \; ; \; |\lambda'_{\rm sf}| = \left| \frac{1}{1 + m \gamma'_{\rm sf} \Delta t} \right| < 1. \tag{102}$$

5.3. Time step size and cycling period for implicit algorithm

As pointed out in [153], even though we adopt quadratic interpolation for the displacement and linear interpolations for all other fields, the solution may still result in oscillatory results if Δt is small. In this section, by employing the implicit backward Euler method (i.e., $\beta_{up} = \beta_{sf} = 1$), we suggest the optimal sizes for Δt and the cycling period m for the mixed time integration scheme that may completely avoid the spurious oscillations by adopting more restrictive conditions. The first condition is the discrete maximum principle (DMP) that requires the positivity (or negativity) of an incremental solution if the right hand side in Eqs. (106)–(108) is positive (or negative), while the second condition requires the monotonicity of the solution, which is called the monotonicity principle (MP) [128–130]. For a system of equation, e.g., $\bar{\bf A} {\bf x} = {\bf b}$, Li and Wei [131] pointed out that both DMP and MP are satisfied if the coefficient matrix $\bar{\bf A}$ is an M-matrix [154,155] that satisfies:

$$\bar{\mathbf{A}}_{ii} > 0 \text{ (no sum)} \; ; \; \bar{\mathbf{A}}_{ii} \le 0 \; (i \ne j).$$

In other words, in order to ensure non-oscillatory results, the diagonal components of the coefficient matrices should be positive while the off-diagonal terms should be non-positive.

Since the asynchronous isothermal split scheme [i.e., case (c) in Fig. 3] solves the decoupled systems separately, we apply the criteria in Eq. (103) to each coefficient matrices to suggest the optimal time step size and the cycling period. By revisiting Eqs. (70)–(73) and Eq. (83)(a), the backward Euler method yields the following expression for the isothermal poromechanics problem:

$$\mathbf{K}\mathbf{u}^{n+1} = \mathbf{G}\mathbf{p}^{n+1} + \mathbf{f}_{\mathbf{u}}^{n+1} + \mathbf{P}\hat{\mathbf{T}}_{\mathbf{s}},\tag{104}$$

$$\mathbf{G}^{\mathrm{T}}\mathbf{u}^{\mathrm{n}+1} + (\mathbf{C} + \Delta t \mathbf{\Phi})\mathbf{p}^{\mathrm{n}+1} = \mathbf{G}^{\mathrm{T}}\mathbf{u}^{\mathrm{n}} + \mathbf{C}\mathbf{p}^{\mathrm{n}} + \Delta t (\mathbf{f}_{\mathrm{n}}^{\mathrm{n}+1} + \mathbf{H}\hat{\mathbf{T}}_{\mathrm{s}}). \tag{105}$$

Substituting Eq. (104) into Eq. (105) yields,

$$\underbrace{(\mathbf{G}^{\mathrm{T}}\mathbf{K}^{-1}\mathbf{G} + \mathbf{C} + \Delta t \mathbf{\Phi})}_{=\tilde{\mathbf{A}}_{\mathrm{up}}} \mathbf{p}^{\mathrm{n+1}} = \mathbf{G}^{\mathrm{T}}\mathbf{u}^{\mathrm{n}} + \mathbf{C}\mathbf{p}^{\mathrm{n}} - \mathbf{G}^{\mathrm{T}}\mathbf{K}^{-1}(\mathbf{f}_{\mathrm{u}}^{\mathrm{n+1}} + \mathbf{P}\hat{\mathbf{T}}_{\mathrm{s}}) + \Delta t(\mathbf{f}_{\mathrm{p}}^{\mathrm{n+1}} + \mathbf{H}\hat{\mathbf{T}}_{\mathrm{s}}).$$
(106)

Similarly, the heat transfer problem can be re-expressed as follows:

$$\underbrace{[\mathbf{S}_{s} + \Delta t(\mathbf{Q}_{s} + \mathbf{E}_{s})]}_{=\tilde{\mathbf{A}}_{s}} \mathbf{T}_{s}^{n+1} = \mathbf{S}_{s} \mathbf{T}_{s}^{n} + \Delta t(\mathbf{D} \mathbf{T}_{f}^{n+1} + \mathbf{f}_{s}^{n+1}), \tag{107}$$

$$\underbrace{[\mathbf{S}_{f} + m\Delta t(\mathbf{A} + \mathbf{Q}_{f} + \mathbf{E}_{f})]}_{=\bar{\mathbf{A}}_{f}} \mathbf{T}_{f}^{n+1} = \mathbf{S}_{f} \mathbf{T}_{f}^{n} + m\Delta t(\mathbf{D}^{T} \mathbf{T}_{s}^{n+1} + \mathbf{f}_{f}^{n+1}).$$
(108)

Here, although we solve for $\{T_s, T_f\}$ simultaneously at the synchronized step (Fig. 4), we consider the decoupled situation to investigate their coefficient matrices separately. In this case, Eqs. (106)–(108) are discrete linear equations to be solved, where the coefficient matrices are: \bar{A}_{up} , \bar{A}_s , and \bar{A}_f . Notice that the diagonal components of the coefficient matrix are positive so that the first criterion in Eq. (103) is automatically satisfied.

In order to illustrate the idea behind our suggestions, we explore the most simple one-dimensional case, while we neglect the heat convection term for simplicity. Since we adopt the Taylor–Hood finite element for the displacement and pore pressure, and linear element for the solid and fluid temperatures, exact Gauss quadrature yields the

following off-diagonal terms of element coefficient matrices $\bar{\mathbf{A}}^e_{\mathrm{up},ij}, \bar{\mathbf{A}}^e_{\mathrm{s},ij}$, and $\bar{\mathbf{A}}^e_{\mathrm{f},ij}$ ($i \neq j$), if $\tau_{\mathrm{SUPG}} \to 0$:

$$\bar{\mathbf{A}}_{\text{up},ij}^{e} = \frac{h_e}{6M^*} - \frac{h_e B^{*2}}{6C^*} - \Delta t \left(\frac{k}{h_e \mu_f}\right),\tag{109}$$

$$\bar{\mathbf{A}}_{s,ij}^{e} = \frac{h_e \rho^s c_s}{6} + \Delta t \left(\frac{h_e a_m h_m}{6} - \frac{\phi^s \kappa_s}{h_e} \right),\tag{110}$$

$$\bar{\mathbf{A}}_{f,ij}^{e} = \frac{h_e \rho^f c_f}{6} + m \Delta t \left(\frac{h_e a_m h_m}{6} - \frac{\phi^f \kappa_f}{h_e} \right), \tag{111}$$

where C^* and k indicate the scalar stiffness and permeability coefficients, respectively. Then, applying the second criterion in Eq. (103) to Eqs. (109)–(111), we get:

$$\Delta t \ge \underbrace{\frac{h_e^2 \mu_f}{k} \left(\frac{1}{6M^*} - \frac{B^{*2}}{6C^*} \right)}_{-\Delta t_{max}},\tag{112}$$

$$\Delta t \ge \underbrace{\frac{h_e^2 \rho^s c_s}{6\phi^s \kappa_s - h_e^2 a_m h_m}}_{=\Delta t_{s,min}},\tag{113}$$

$$m\Delta t \ge \underbrace{\frac{h_e^2 \rho^f c_f}{6\phi^f \kappa_f - h_e^2 a_m h_m}}_{=\Delta \kappa_{min}},\tag{114}$$

respectively. This 1D example underscores that the minimum time step size Δt for the mixed time integration should satisfy Eqs. (112)–(114) at the same time. Also notice that, unless employing a different interpolation strategy, the criteria remain the same in two- or three-dimensional cases, while $\Delta t_{\rm up,min}$, $\Delta t_{\rm s,min}$, and $\Delta t_{\rm f,min}$ may have different expressions depending on the spatial dimension.

Overall, for the asynchronous isothermal splitting scheme shown in Fig. 4, we propose the following general criteria for the cycling period m as:

$$m \approx \frac{\rho_f c_f \kappa_s}{\rho_s c_s \kappa_f},\tag{115}$$

so that $m\Delta t_{\rm s,min} \approx \Delta t_{\rm f,min}$, while the time step size can be chosen as,

$$\Delta t \ge \max(\Delta t_{\text{up,min}}, \Delta t_{\text{s,min}}).$$
 (116)

To be conservative, we set Δt one to two orders of magnitudes larger than max ($\Delta t_{\rm up,min}$, $\Delta t_{\rm s,min}$) for all the numerical examples in Section 6.

Remark 3. The phase field approach to fracture requires a mesh that is locally refined along the potential crack path, where element sizes may substantially vary over the domain. For a thermo-hydro-mechanical-fracture problem that involves high pressure or temperature gradients near the crack, $\Delta t_{\rm up,min}$ and $\Delta t_{\rm s,min}$ in Eqs. (112) and (113) can be determined by using the minimum element size, i.e., min (h_e) , in order to capture the detailed coupled processes near damaged regions.

6. Numerical examples

This section presents three sets of numerical examples to showcase the capacities of the proposed model, focusing on transient problems that involve heat exchange between the solid and fluid constituents. We limit our attention to one- or two-dimensional simulations at cm-scale and neglect the gravitational effects (i.e., g=0), while adopting implicit backward Euler time integration scheme with a Newton-Raphson solver. As a preliminary study, the first example compares three different time integration schemes illustrated in Fig. 3 by simulating one-dimensional heat transfer process in a water-saturated porous column to demonstrate the computational efficiency of the asynchronous isothermal split solution scheme. In the second numerical example, we compare the one-temperature model that considers local thermal equilibrium (LTE) state with the two-temperature model where the

Table 1
Material parameters for one-dimensional heat conduction problem.

Parameter	Description [Unit]	Value
ρ_s	Intrinsic solid mass density [kg/m ³]	2700.0
$ ho_f$	Intrinsic fluid mass density [kg/m ³]	1000.0
K_s	Bulk modulus of solid constituent [Pa]	40.0×10^{9}
K_f	Bulk modulus of pore fluid [Pa]	2.1×10^{9}
c_s	Specific heat of solid constituent [J/kg/K]	1.0×10^{3}
c_f	Specific heat of pore fluid [J/kg/K]	4.2×10^{3}
κ_s	Thermal conductivity of solid constituent [W/m/K]	4.2
κ_f	Thermal conductivity of pore fluid [W/m/K]	0.6
α_s	Linear thermal expansion coefficient of solid constituent [1/K]	10.0×10^{-6}
A_{μ}	Viscosity parameter [Pa s]	1.1×10^{-6}
B_{μ}	Viscosity parameter [K]	2005.3
$T_{s,\mathrm{ref}}$	Reference solid temperature [K]	293.15
E	Elastic modulus of solid skeleton [Pa]	18.0×10^{9}
ν	Poisson's ratio of solid skeleton [-]	0.2
k_{mat}	Matrix permeability [m ²]	1.0×10^{-17}
ϕ_{ref}^f	Reference porosity [-]	0.2
$a_{m,\mathrm{ref}}$	Reference specific surface area [1/m]	20.0
h_m	Heat transfer coefficient [W/m ² K]	4.7

solid and fluid constituents are in local thermal non-equilibrium (LTNE). Specifically, we focus on the effect of the different growth rates of thermal boundary layers on the fracture pattern by simulating a mechanically driven crack propagation on an oil-saturated double-edge-notched specimen. Finally, the third example highlights the modeling capacity of capturing the coupled thermo-hydro-mechanical-fracture processes by simulating the interaction of two cracks that are hydraulically stimulated by injecting hot fluid into pre-existing flaws. The implementation of the model including the finite element discretization and the solution scheme relies on the finite element package FEniCS [156–158] with PETSc scientific computational toolkit [159], while all the numerical simulations rely on meshes that are sufficiently refined around the potential crack trajectory in order to capture the damage field around crack surfaces properly.

6.1. Comparative study: one-dimensional heat transfer

This example simulates the one-dimensional heat transfer process in a porous column by prescribing a raised temperature at the top surface. Assuming that the solid and fluid constituents are in LTNE state and remain undamaged, this numerical example serves as a preliminary study that compares the performance between three different time integration schemes shown in Fig. 3.

In this example, we choose the material properties of the problem domain similar to a typical water-saturated sandstone, which is summarized in Table 1. As illustrated in Fig. 5, our 0.1 m long porous column with initial temperatures of $\theta_{s0} = \theta_{f0} = 20$ °C is subjected to thermal loading of $\hat{\theta}_s = \hat{\theta}_f = 50$ °C at the top, while we impose fixed temperature boundary conditions $\hat{\theta}_s = \hat{\theta}_f = 20$ °C at the bottom. During the simulation, the bottom part of the porous column is held fixed and is subjected to a zero pore pressure boundary condition, whereas no fluid flux is allowed at the top. Within this setup, we conduct a number of numerical experiments by using three different time integration schemes (i.e., monolithic, isothermal split, and asynchronous isothermal split). By spatially discretizing the domain into uniform elements with $h_e = 0.4$ mm, we have: $\Delta t_{\rm up,min} \approx 0.09$ s and $\Delta t_{\rm s,min} \approx 0.02$ s from Eqs. (112)–(113). Hence, from Eq. (116), we choose $\Delta t = 5$ s for all three solution schemes, while we set the cycling period as m = 10 for the asynchronous isothermal splitting scheme since $\rho_f c_f \kappa_s/\rho_s c_s \kappa_f = 10.88$.

Fig. 6 shows the variations of displacement, pore pressure, solid temperature, and fluid temperature along the height of the column. Here, circular and triangular symbols indicate the results obtained from the monolithic and isothermal splitting solvers, respectively, whereas square symbols denote the simulation results from the asynchronous isothermal split solver. As illustrated in Figs. 6(c) and 6(d), the solid constituent tends to conduct heat better than the fluid phase, while the fluid heat transfer process is accelerated as time proceeds due to the

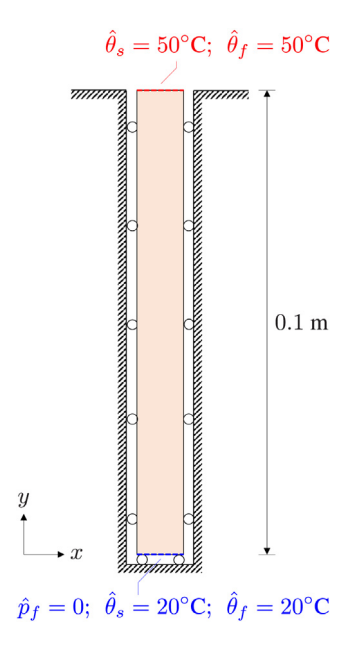


Fig. 5. Schematic of geometry and boundary conditions for the one-dimensional heat transfer problem.

heat exchange between two constituents. Also, due to the thermal loads, the porous matrix experiences thermal expansion that leads to the build-up of pore pressure which dissipates over time, as shown in Figs. 6(a) and 6(b). Although the good agreement between the solutions obtained by different time integration schemes confirms the validity of the proposed solution strategy, there exists a noticeable time lagging error for θ_f at t = 100 s [Fig. 6(d)]. As illustrated in Fig. 7, this time lagging error may lead to inaccurate results at an earlier stage if we use large m even though it becomes marginal as time goes on. However, it should be noted that choosing a cycling period smaller than our suggestion in Eq. (115) may either prevent proper utilization of computational efficiency of the asynchronous time integration scheme, or result in spurious oscillations since it may violate the discrete maximum principle (DMP) or monotonicity principle (MP) even if the time step size is greater than max ($\Delta t_{\rm up,min}$, $\Delta t_{\rm s,min}$).

Based on this experimental setup, we further quantitatively analyze the computational efficiency of the asynchronous isothermal splitting scheme. In order to do so, we repeat the same set of numerical experiments with different spatial and temporal discretizations, and record their CPU times. Specifically, by adopting a cycling period of m=10, we investigate the effect of element size h_e by using different meshes with the same $\Delta t=10$ s, whereas the effect of time stepping size is examined by conducting the simulations with different Δt while element size is set to be $h_e=0.04$ mm. Here, the numerical simulations are conducted on a single core of Intel i9-9880H processor with 16 GB memory at 2667 MHz (DDR4), while we use the same convergence tolerances for all the Newton–Raphson iterations.

Fig. 8 illustrates the measured computational costs for the monolithic (circular symbols), isothermal split (triangular symbols), and asynchronous isothermal split (square symbols) solution schemes. As illustrated in Figs. 8(a) and 8(b), the observed CPU times are inversely proportional to both the element size h_e and the time step size Δt , indicating that both the spatial and temporal refinements increase computational costs. In both two cases, we observe that the monolithic scheme is the most computationally expensive approach, while the isothermal split and asynchronous isothermal split schemes require ~ 72 % and ~ 60 % less CPU times, respectively, compared to the monolithic solver. This time saving can be attributed to the reduced number of calculation afforded by the asynchronous time steps. On the other hand, it can also be related to the larger system of equation and the higher condition number of the tangential matrix of the monolithic solver. The results highlight that our proposed asynchronous isothermal splitting scheme yields similar results compared to the other two approaches, while being computationally more efficient.

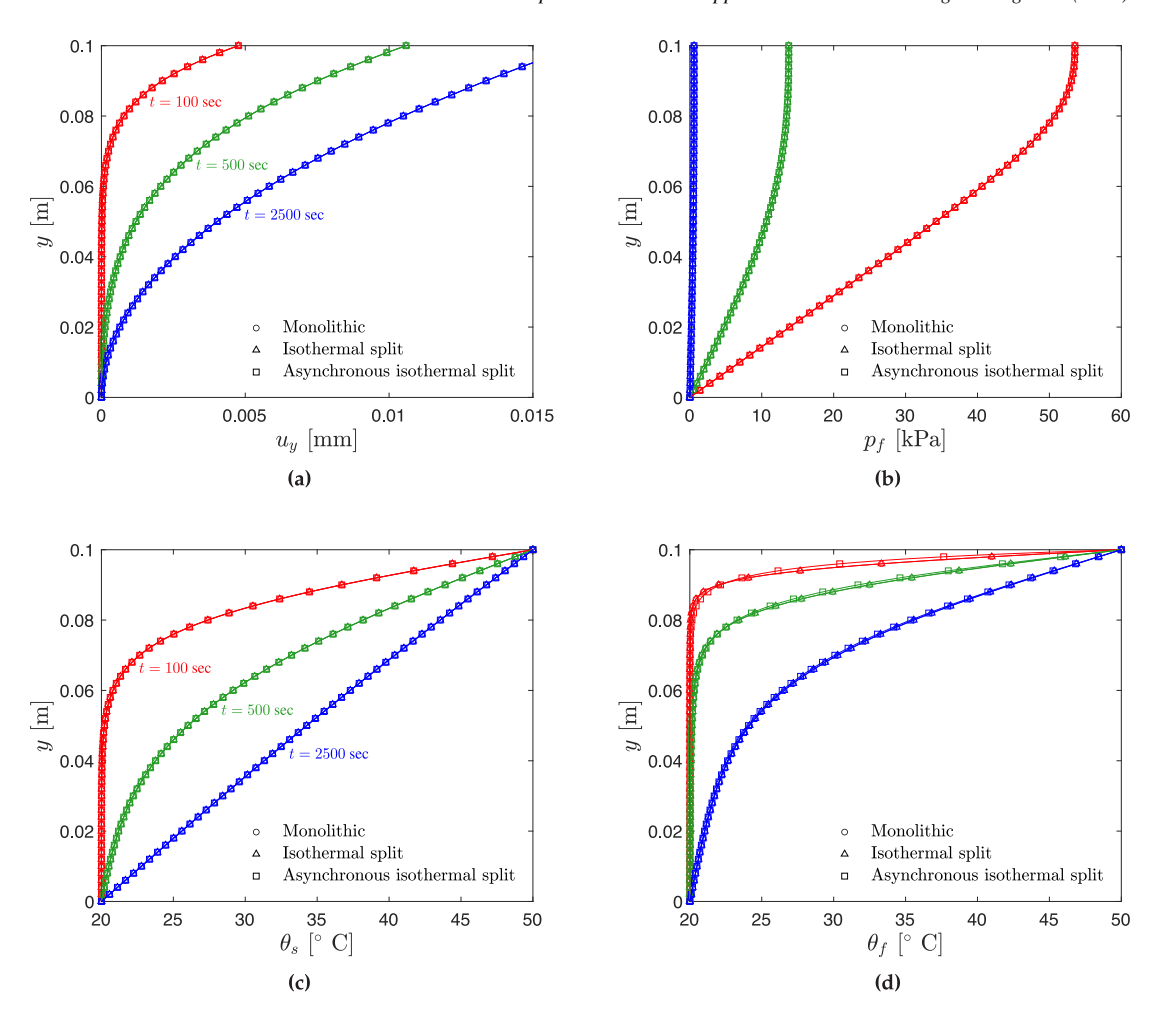


Fig. 6. Transient responses of porous column. (a) displacement; (b) pore pressure; (c) solid temperature; and (d) fluid temperature.

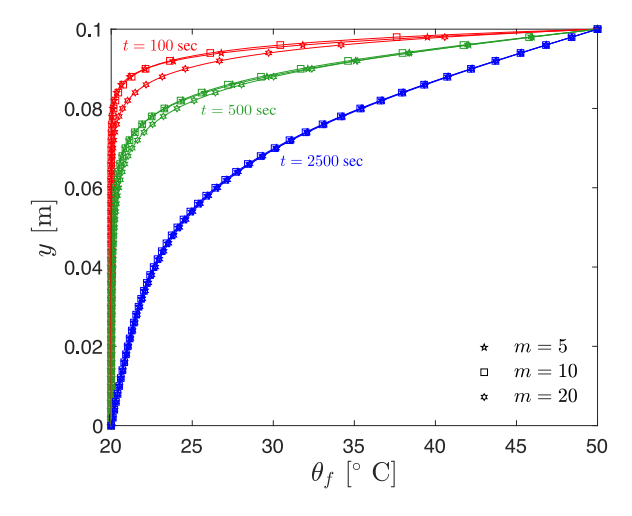


Fig. 7. Evolution of θ_f obtained from the asynchronous isothermal split solution scheme with different cycling periods.

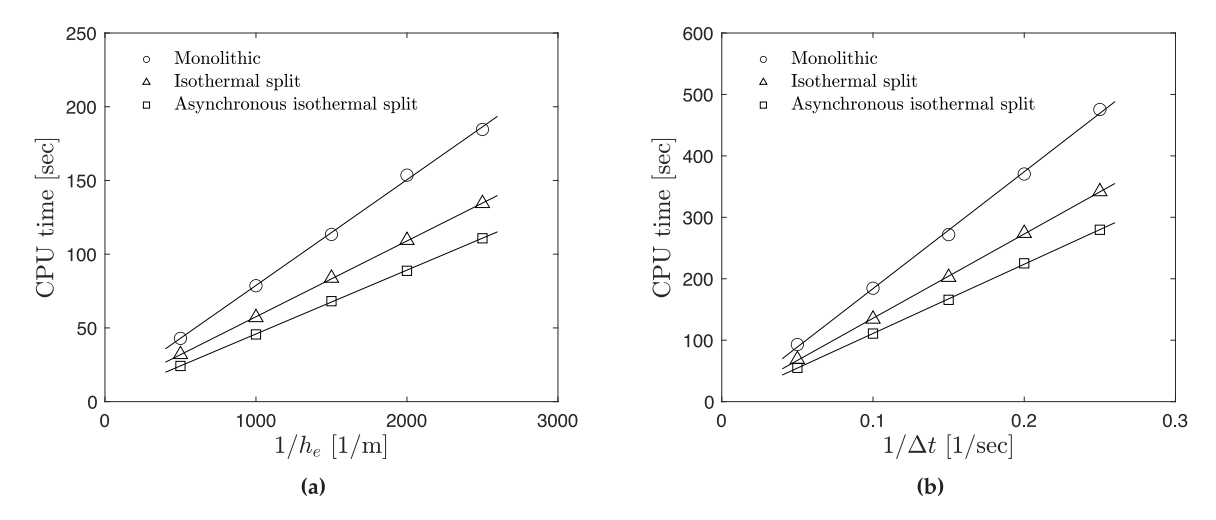


Fig. 8. Performance comparison between different time integration schemes. (a) CPU time vs. $1/h_e$, and (b) CPU time vs. $1/\Delta t$.

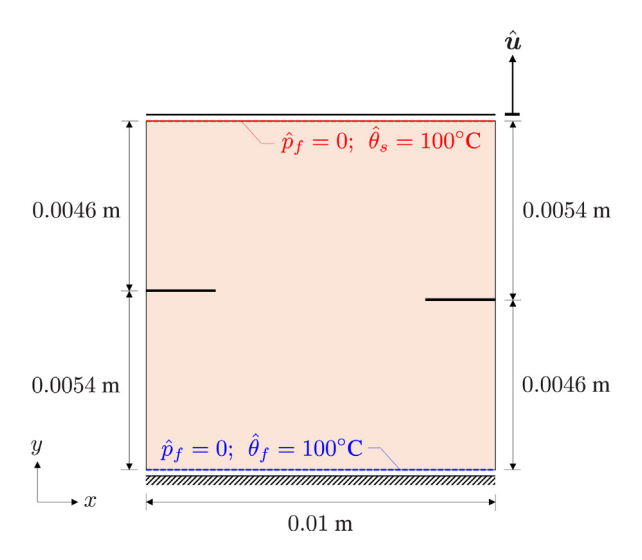


Fig. 9. Schematic of geometry and boundary conditions for the tension test.

6.2. Interaction of two mechanically driven cracks

This numerical example investigates the effect of thermally non-equilibrated constituents (i.e., LTNE) on the fracture pattern due to different growth rates of thermal boundary layers compared to the one-temperature model that assumes LTE state. For the case where two constituents are in LTE state, we replace Eqs. (30) and (33) with Eq. (34) by adopting an isothermal splitting scheme with a single time step, while two-temperature approach adopts the proposed asynchronous isothermal operator split.

As illustrated in Fig. 9, the problem domain is 0.01 m wide and 0.01 m long square plate with two 0.002 m long asymmetric horizontal edge notches, while we choose the material properties similar to an oil-saturated rock which is summarized in Table 2. While the initial temperatures are set to be 20 °C (i.e., $\theta_{m0} = 20$ °C for the one-temperature model and $\theta_{s0} = \theta_{f0} = 20$ °C for the two-temperature model), we impose zero pore pressure and fixed temperature boundary conditions at the top (i.e., $\hat{\theta}_m = 100$ °C for the one-temperature model and $\hat{\theta}_s = 100$ °C for the two-temperature model and $\hat{\theta}_f = 100$ °C for the two-temperature model. Within this setup, we conduct numerical experiments, where the crack growth from the pre-existing notches is mechanically driven, by prescribing vertical displacement at the top at a rate of

Table 2Material parameters for the tension test.

Parameter	Description [Unit]	Value
ρ_s	Intrinsic solid mass density [kg/m ³]	2600.0
$ ho_f$	Intrinsic fluid mass density [kg/m ³]	880.0
K_s	Bulk modulus of solid constituent [Pa]	38.0×10^{9}
K_f	Bulk modulus of pore fluid [Pa]	1.3×10^{9}
c_s	Specific heat of solid constituent [J/kg/K]	1.0×10^{3}
c_f	Specific heat of pore fluid [J/kg/K]	2.0×10^{3}
κ_s	Thermal conductivity of solid constituent [W/m/K]	4.2
κ_f	Thermal conductivity of pore fluid [W/m/K]	0.15
α_s	Linear thermal expansion coefficient of solid constituent [1/K]	12.0×10^{-6}
A_{μ}	Viscosity parameter [Pa s]	8.6×10^{-6}
B_{μ}	Viscosity parameter [K]	2475.5
$T_{s,\mathrm{ref}}$	Reference solid temperature [K]	293.15
E	Elastic modulus of solid skeleton [Pa]	18.0×10^{9}
ν	Poisson's ratio of solid skeleton [-]	0.25
k_{mat}	Matrix permeability [m ²]	2.5×10^{-16}
$\phi_{ ext{ref}}^f$	Reference porosity [-]	0.3
$a_{m,\mathrm{ref}}$	Reference specific surface area [1/m]	20.0
h_m	Heat transfer coefficient [W/m ² K]	4.7
$\mathcal{G}_{c,\mathrm{ref}}$	Reference critical energy release rate [N/m]	20.0
a_c	Model parameter [–]	1.0
l_c	Regularization length scale parameter [m]	0.45×10^{-4}

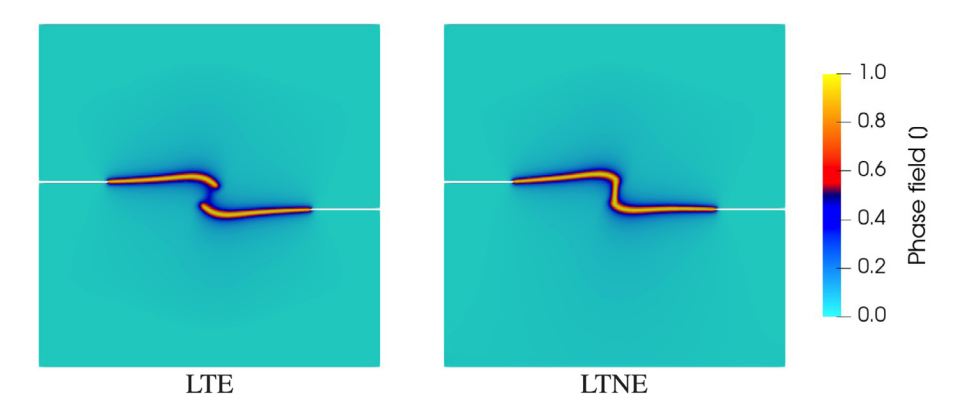


Fig. 10. Snapshots of the phase fields obtained from the tension tests by using the one-temperature (LTE) and two-temperature (LTNE) models at t = 1.8 s.

 0.75×10^{-5} m/s whereas the bottom part is held fixed during the simulation. The problem domain is spatially discretized with a mesh which is refined along the potential crack path with min $(h_e) = 1.5 \times 10^{-5}$ m, while we use max $(h_e) = 2.0 \times 10^{-4}$ m near the external boundaries. Hence, we choose $\Delta t = 0.005$ s > max $(\Delta t_{\rm up,min}, \Delta t_{\rm s,min})$ for both two cases (i.e., LTE and LTNE), while the cycling period for the two-temperature model is set to be m = 20 since $\rho_f c_f \kappa_s / \rho_s c_s \kappa_f = 18.95$.

Fig. 10 illustrates the crack trajectories at t = 1.8 s for both cases where the constituents are in LTE and LTNE states. As shown in Fig. 11(a), two models exhibit a different growth rates of thermal boundary layers, since the two-temperature model is capable of imposing separate temperature boundary conditions for each constituent. In specific, the limitation of the LTE assumption yields the symmetric thermal boundary layer growth of equilibrated temperature θ_m that leads to symmetric crack growth, while the asymmetric distributions of two temperatures in LTNE state tend to break the symmetry of crack propagation from the notches and eventually coalescence toward each other, resulting in different global responses shown in Fig. 11(b). In addition, as illustrated in Fig. 12, due to the discrepancy between the peaks shown in Fig. 11(b), the LTE model tends to exhibit higher negative pore

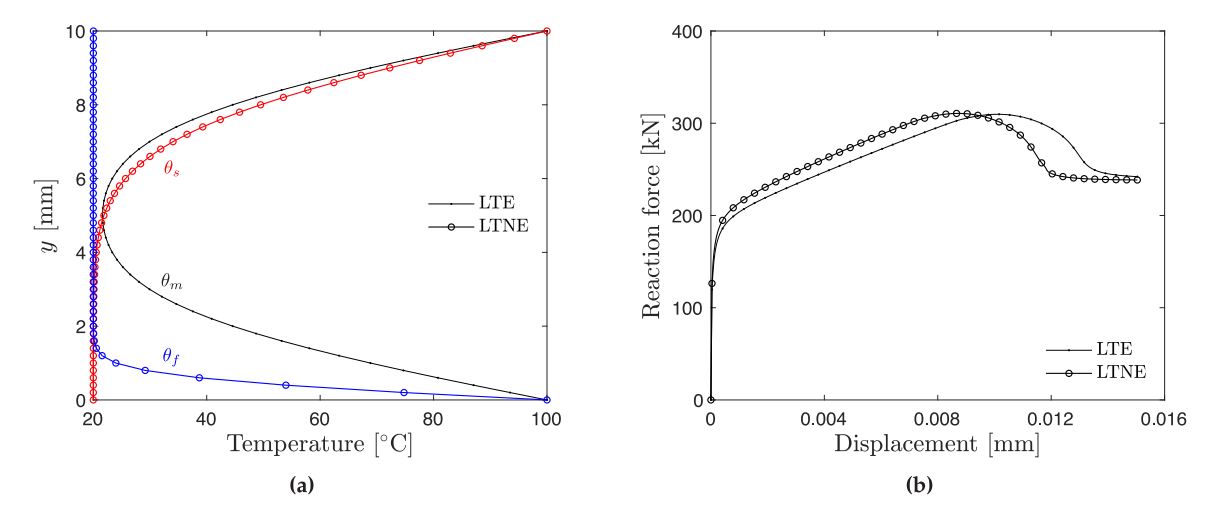


Fig. 11. (a) Distribution of the temperatures along the center axis of the specimen at t = 1.5 s, and (b) force–displacement curves from the tension tests.

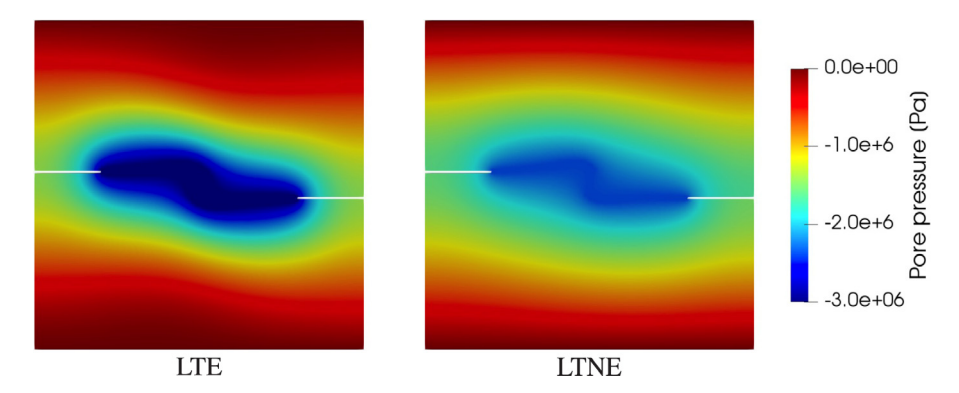


Fig. 12. Snapshots of the pore pressure fields obtained from the tension tests obtained from the one-temperature (LTE) and two-temperature (LTNE) models at t = 1.8 s.

pressure compared to the LTNE model at t=1.8 s, even though the LTE assumption may underestimate the temperature-dependent viscosity μ_f .

6.3. Interaction of two hydraulically induced cracks

This section simulates the interaction of two hydraulically induced cracks by injecting hot fluid into pre-existing notches. As illustrated in Fig. 13(a), the 0.2 m × 0.1 m sized rectangular domain possesses two 0.02 m long edge notches that are perpendicular to each other with a distance of 0.01 m. The crack growth from the notches is triggered by injecting hot water ($\hat{\theta}_f = 100$ °C) with a rate of $A_c\hat{s}$ into a cold water-saturated medium with initial temperatures of $\theta_{s0} = \theta_{f0} = 0$ °C. Here, the total area of the pre-existing notches is set to be $A_c = 16$ mm² while the applied fluid source varies with time, i.e., $\hat{s} = \hat{s}(t)$, as shown in Fig. 13(b). This scenario is designed to capture both the hydraulic fracturing process and the post-cracking behavior of the material. We first apply the fluid source at a constant rate of $\hat{s} = 0.1$ s⁻¹ during the fracturing stage ($t \le 1$ s), and then smoothly reduce the injection rate by applying $\hat{s} = 0.05 + 0.025/(t - 0.5)$ s⁻¹ at the injecting stage ($t \ge 1$ s). During the simulation, all the external boundaries are held fixed and are subjected to zero pore pressure and zero temperature boundary conditions, i.e., $\hat{\rho}_f = 0$ and $\hat{\theta}_s = \hat{\theta}_f = 0$ °C, while the chosen material parameters are summarized in Table 3.

Similar to Section 6.2, we compare the one- and two-temperature models within this experimental setup. Since this example relies on a mesh that possesses $\min(h_e) = 0.36$ mm, we choose $\Delta t = 0.01$ s > $\max(\Delta t_{\text{up,min}}, \Delta t_{\text{s,min}})$

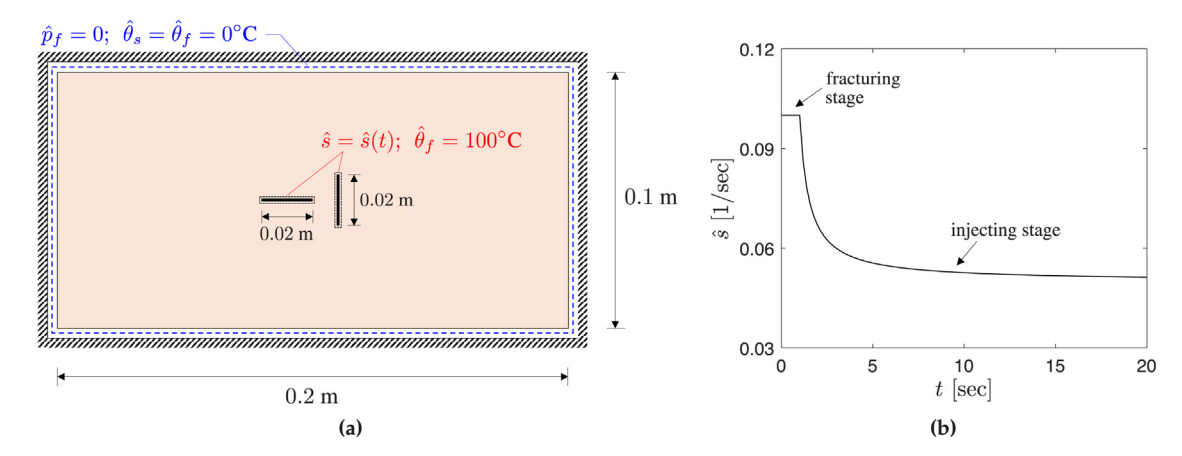


Fig. 13. (a) Schematic of geometry and boundary conditions for the injection problem, and (b) applied fluid source along the pre-existing cracks.

Table 3
Material parameters for the injection problem.

Parameter	Description [Unit]	Value
ρ_{s}	Intrinsic solid mass density [kg/m ³]	2700.0
$ ho_f$	Intrinsic fluid mass density [kg/m ³]	1000.0
K_s	Bulk modulus of solid constituent [Pa]	40.0×10^9
K_f	Bulk modulus of pore fluid [Pa]	2.1×10^{9}
c_s	Specific heat of solid constituent [J/kg/K]	1.0×10^{3}
c_f	Specific heat of pore fluid [J/kg/K]	4.2×10^{3}
κ_s	Thermal conductivity of solid constituent [W/m/K]	4.2
κ_f	Thermal conductivity of pore fluid [W/m/K]	0.6
α_s	Linear thermal expansion coefficient of solid constituent [1/K]	10.0×10^{-6}
A_{μ}	Viscosity parameter [Pa s]	1.1×10^{-6}
B_{μ}	Viscosity parameter [K]	2005.3
$T_{s,\mathrm{ref}}$	Reference solid temperature [K]	273.15
E	Elastic modulus of solid skeleton [Pa]	25.0×10^9
ν	Poisson's ratio of solid skeleton [-]	0.3
k_{mat}	Matrix permeability [m ²]	1.25×10^{-16}
$\phi_{ ext{ref}}^f$	Reference porosity [–]	0.2
$a_{m,\mathrm{ref}}$	Reference specific surface area [1/m]	20.0
h_m	Heat transfer coefficient [W/m ² K]	4.7
$\mathcal{G}_{c,\mathrm{ref}}$	Reference critical energy release rate [N/m]	20.0
a_c	Model parameter [-]	1.0
l_c	Regularization length scale parameter [m]	1.25×10^{-3}

for both two models, i.e., LTE and LTNE, and we set the cycling period m=10 for the two-temperature model as the chosen material parameters yield: $\rho_f c_f \kappa_s / \rho_s c_s \kappa_f = 10.88$.

Fig. 14 shows the crack patterns at different time steps, obtained from both the LTE and LTNE models, while corresponding pore pressure fields are shown in Fig. 15. The crack growth simulated by both the one- and two-temperature models reach their final configurations at $t \approx 1.4$ s as we reduce the injection rate after t = 1 s. As illustrated in Fig. 16, for the case where two constituents are in LTNE state, the boundary layer of the solid temperature grows at a much slower rate compared to the fluid temperature since the heat transfer process is convection-dominant. On the other hand, the LTE model tends to convect heat similar to the LTNE model, while it overestimates the diffusivity due to the difference in the diffusion coefficients, resulting in different patterns of temperature evolution. More importantly, Eq. (11) hints that the two-temperature model accumulates the effective strain energy ψ' around the cracks at a higher rate compared to the one-temperature model. The cracks therefore

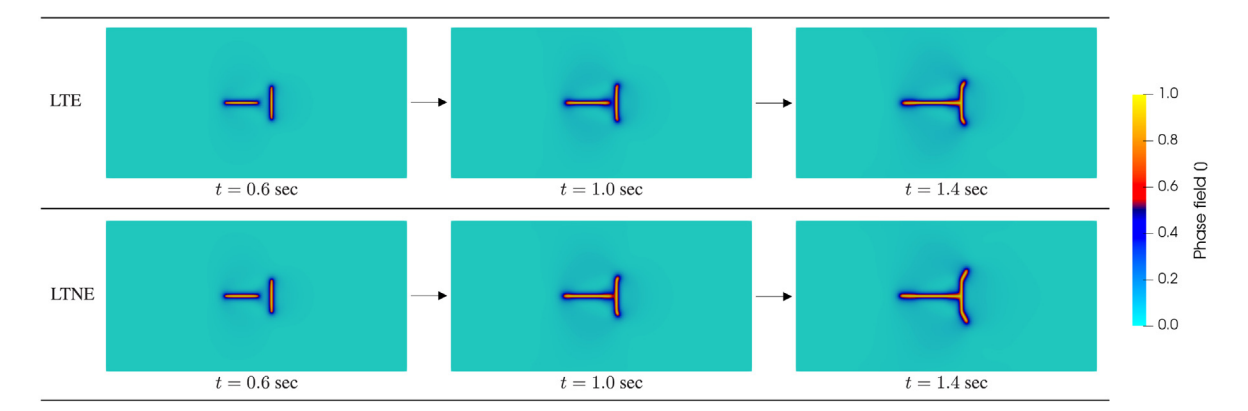


Fig. 14. Evolution of the phase field due to fluid injection obtained from the one-temperature (LTE) and two-temperature (LTNE) models.

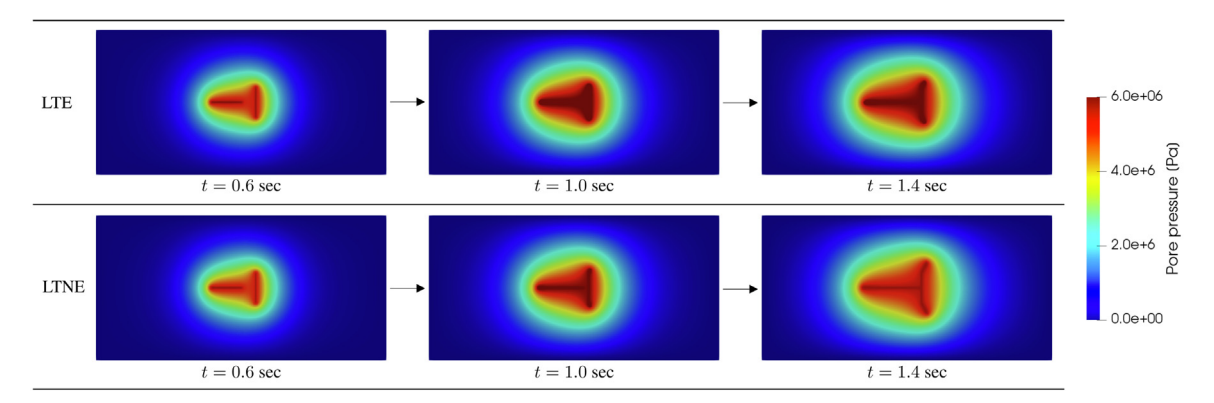


Fig. 15. Pore pressure evolution due to the field injection obtained from the one-temperature (LTE) and two-temperature (LTNE) models.

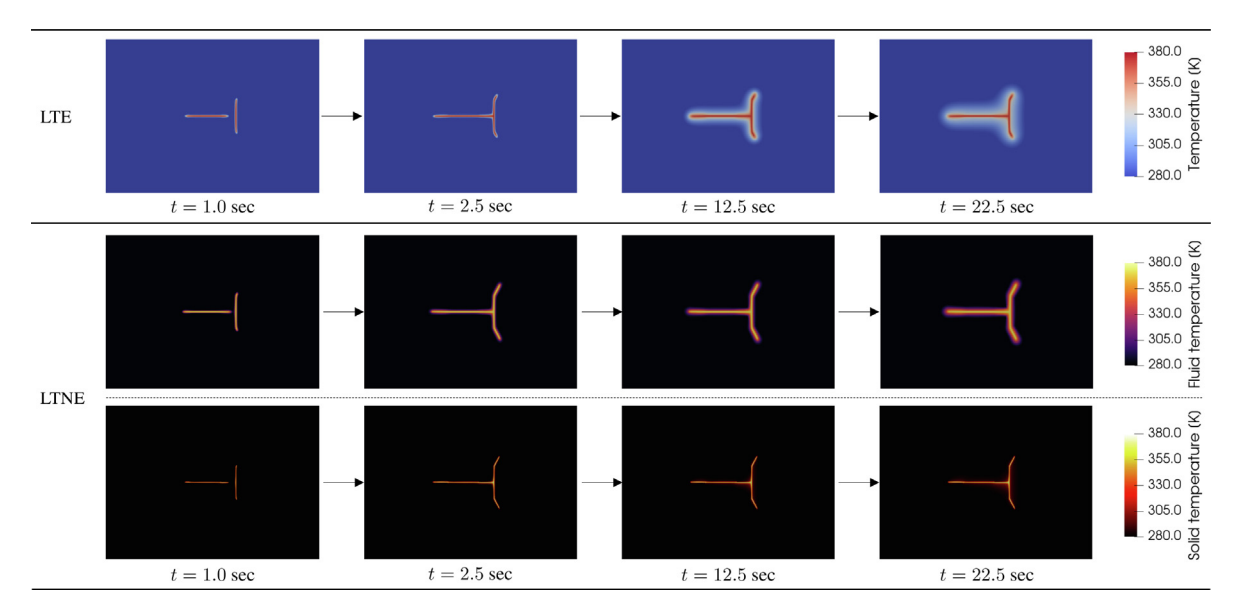


Fig. 16. Evolution of temperature fields due to the fluid injection obtained from the one-temperature (LTE) and two-temperature (LTNE) models.

start to propagate at earlier time steps in LTNE state (Fig. 14), resulting in a faster rate of pore pressure dissipation (Fig. 15).

7. Conclusions and future perspective

In this study, we present a phase field framework that captures the coupled thermo-hydro-mechanical processes of brittle porous media and propose an asynchronous time integrator to handle the diffusion process that spans different time scales. To the best of the authors' knowledge, this is the first mathematical framework that captures the brittle fracture in multi-phase fluid-infiltrating porous media where the constituents are in a local thermal non-equilibrium state. By introducing a new effective medium theory that independently homogenizes the constituent temperatures, we provide a theoretical basis for distinctive energy balance equations for each deformable constituent, while capturing the heat exchange between the two thermally connected constituents. The two-temperature poromechanics model presented in this work is a generalization of the one-temperature model in the sense that the results of the classical one-temperature model can be recovered by assuming that all the constituents instantly reach a local thermal equilibrium. By explicitly modeling the heat transfer of the two constituents, we bypass the need to homogenize the intrinsic specific heat capacities and thermal conductivities of each constituent. This treatment simplifies the calibration process, which is by no mean trivial for porous media where the motions of the fluid and solid constituents do not coincide and the conductivity of the effective medium are not necessarily isotropic. In addition, we propose a new time integration scheme that updates the field variables in an asynchronous manner, for which we also suggest an estimated optimal time step size and cycling period by adopting the discrete maximum and monotonicity principles. The asynchronous time integrator greatly reduces the computational cost, while being capable of reproducing physically consistent results with the synchronous counterpart.

Note that a more precise and accurate calculation of heat transfer will have an even more profound effect on poromechanics problems with phase transitions of either/both the solid and fluid constituents, such as the freeze-thaw action in soil and rock, crystallization induced damage and injection of supercritical CO₂. The proposed work may lay the groundwork for a more precise predictions for those important problems without the necessity of additional calibrations of the thermal diffusivity of the effective medium. Another future work of this study is to simulate three dimensional cases. A major challenge for 3D simulations of the phase field fracture in the non-equilibrium porous media is the computational effort. Accurately representing the crack growth via phase field will require a sufficiently high mesh resolution and small time step, which can be computationally demanding. At this point we are considering a more efficient parallelism that involves GPGPU as well as adaptive finite element that involves proper way to project the driving force. Works in these areas are currently in progress.

Declaration of competing interest

The authors declare that they have no known competing financial interests or personal relationships that could have appeared to influence the work reported in this paper.

Code and data availability statement

The source codes and data generated during and/or analyzed during the current study are available from the corresponding author upon reasonable request.

Acknowledgments

The authors thank the three anonymous reviewers for the constructive feedback and suggestions. This work is supported by the Earth Materials and Processes program from the US Army Research Office under grant contract W911NF-18-2-0306 and the NSF CAREER grant from Mechanics of Materials and Structures program at National Science Foundation, USA under grant contract CMMI-1846875. These supports are gratefully acknowledged. The views and conclusions contained in this document are those of the authors, and should not be interpreted as representing the official policies, either expressed or implied, of the sponsors, including the Army Research Laboratory or the U.S. Government. The U.S. Government is authorized to reproduce and distribute reprints for Government purposes notwithstanding any copyright notation herein.

Appendix. Finite element discretization

Here, we present the weak form of the governing field equations, and then develop a semi-discrete formulation for the numerical solution of the thermo-hydro-mechanical and phase field fracture model we described in Sections 3 and 4. We start by summarizing the governing equations and the relevant initial boundary value problem, and then follow the standard weighted residual procedure to recover the weak form. For robust spatial discretization of the coupled problem, we use the Taylor–Hood finite element space for the displacement and pore pressure fields, and standard linear interpolation for the solid and fluid temperatures, while adopting streamline upwind Petrov–Galerkin (SUPG) stabilization for the fluid phase energy balance equation. Meanwhile, the phase field is also interpolated by linear function to ensure the efficiency of the staggered solver which sequentially updates the phase field and non-isothermal poromechanics problem.

A.1. Weak form

By revisiting Sections 3 and 4, the governing field equations with primary unknowns $\{u, p_f, \theta_s, \theta_f, d\}$ are summarized as follows:

$$\begin{cases} \nabla \cdot \boldsymbol{\sigma} + \rho \boldsymbol{g} = \boldsymbol{0}, \\ \frac{1}{M^*} \dot{p}_f - 3\alpha_s (B^* - \phi^f) \dot{\theta}_s + B^* \nabla \cdot \boldsymbol{v} + \nabla \cdot \boldsymbol{w} = \hat{s}, \\ \rho^s c_s \dot{\theta}_s - \mathcal{D}_{\text{int}}^s + \nabla \cdot \boldsymbol{q}^s + a_m h_m (\theta_s - \theta_f) = \hat{r}^s, \\ \rho^f c_f \dot{\theta}_f + \rho_f c_f (\boldsymbol{w} \cdot \nabla \theta_f) + \nabla \cdot \boldsymbol{q}^f + a_m h_m (\theta_f - \theta_s) = \hat{r}^f, \\ g'(d)\mathcal{H} + (d - l_c^2 \nabla^2 d) = 0, \end{cases}$$
(A.1)

and the prescribed boundary conditions can be specified as,

$$\begin{cases} \boldsymbol{u} = \hat{\boldsymbol{u}} & \text{on } \partial \mathcal{B}_{u} \\ p_{f} = \hat{p}_{f} & \text{on } \partial \mathcal{B}_{p} \\ \theta_{s} = \hat{\theta}_{s} & \text{on } \partial \mathcal{B}_{\theta_{s}} \end{cases}; \begin{cases} \boldsymbol{\sigma} \cdot \boldsymbol{n} = \hat{\boldsymbol{t}} & \text{on } \partial \mathcal{B}_{t} \\ -\boldsymbol{w} \cdot \boldsymbol{n} = \hat{\boldsymbol{w}} & \text{on } \partial \mathcal{B}_{w} \\ -\boldsymbol{q}^{s} \cdot \boldsymbol{n} = \hat{q}_{s} & \text{on } \partial \mathcal{B}_{q^{s}} \end{cases}$$

$$(A.2)$$

$$(A.2)$$

Here, n is the outward-oriented unit normal on the boundary surface $\partial \mathcal{B}$ that consists of Dirichlet boundaries (displacement boundary $\partial \mathcal{B}_u$, pore pressure boundary $\partial \mathcal{B}_p$, solid temperature boundary $\partial \mathcal{B}_{\theta_s}$, and fluid temperature boundary $\partial \mathcal{B}_{\theta_f}$) and Neumann boundaries (traction boundary $\partial \mathcal{B}_t$, fluid flux boundary $\partial \mathcal{B}_w$, solid heat flux boundary $\partial \mathcal{B}_{q^s}$, and fluid heat flux boundary $\partial \mathcal{B}_{q^f}$) satisfying:

$$\partial \mathcal{B} = \overline{\partial \mathcal{B}_u \cup \partial \mathcal{B}_t} = \overline{\partial \mathcal{B}_p \cup \partial \mathcal{B}_w} = \overline{\partial \mathcal{B}_{\theta_s} \cup \partial \mathcal{B}_{q^s}} = \overline{\partial \mathcal{B}_{\theta_f} \cup \partial \mathcal{B}_{q^f}}, \tag{A.3}$$

$$\emptyset = \partial \mathcal{B}_u \cap \partial \mathcal{B}_t = \partial \mathcal{B}_p \cap \partial \mathcal{B}_w = \partial \mathcal{B}_{\theta_s} \cap \partial \mathcal{B}_{q^s} = \partial \mathcal{B}_{\theta_f} \cap \partial \mathcal{B}_{q^f}, \tag{A.4}$$

while the following boundary condition on $\partial \mathcal{B}$ is prescribed for the phase field d:

$$\nabla d \cdot \mathbf{n} = 0. \tag{A.5}$$

For model closure, the initial conditions are imposed as,

$$u = u_0$$
; $p_f = p_{f0}$; $\theta_s = \theta_{s0}$; $\theta_f = \theta_{f0}$; $d = d_0$, (A.6)

at time t = 0. Then, we define the trial spaces V_u , V_p , V_{θ_s} , V_{θ_f} and V_d for the solution variables as follows:

$$V_{u} = \left\{ \boldsymbol{u} : \mathcal{B} \to \mathbb{R}^{n_{\text{dim}}} \mid \boldsymbol{u} \in [H^{1}(\mathcal{B})]^{n_{\text{dim}}}, \ \boldsymbol{u}|_{\partial \mathcal{B}_{u}} = \hat{\boldsymbol{u}} \right\},$$

$$V_{p} = \left\{ p_{f} : \mathcal{B} \to \mathbb{R} \mid p_{f} \in H^{1}(\mathcal{B}), \ p_{f}|_{\partial \mathcal{B}_{p}} = \hat{p}_{f} \right\},$$

$$V_{\theta_{s}} = \left\{ \theta_{s} : \mathcal{B} \to \mathbb{R} \mid \theta_{s} \in H^{1}(\mathcal{B}), \ \theta_{s}|_{\partial \mathcal{B}_{\theta_{s}}} = \hat{\theta}_{s} \right\},$$

$$V_{\theta_{f}} = \left\{ \theta_{f} : \mathcal{B} \to \mathbb{R} \mid \theta_{f} \in H^{1}(\mathcal{B}), \ \theta_{f}|_{\partial \mathcal{B}_{\theta_{f}}} = \hat{\theta}_{f} \right\},$$

$$V_{d} = \left\{ d : \mathcal{B} \to \mathbb{R} \mid d \in H^{1}(\mathcal{B}) \right\},$$

$$(A.7)$$

where n_{dim} is the spatial dimension while H^1 indicates the Sobolev space of order 1. Similarly, the corresponding admissible spaces for Eq. (A.7) are defined as,

$$V_{\eta} = \left\{ \boldsymbol{\eta} : \mathcal{B} \to \mathbb{R}^{\text{n}_{\text{dim}}} \mid \boldsymbol{\eta} \in [H^{1}(\mathcal{B})]^{\text{n}_{\text{dim}}}, \ \boldsymbol{\eta}|_{\partial \mathcal{B}_{u}} = \boldsymbol{0} \right\},$$

$$V_{\xi} = \left\{ \xi : \mathcal{B} \to \mathbb{R} \mid \xi \in H^{1}(\mathcal{B}), \ \xi|_{\partial \mathcal{B}_{p}} = 0 \right\},$$

$$V_{\zeta_{s}} = \left\{ \zeta_{s} : \mathcal{B} \to \mathbb{R} \mid \zeta_{s} \in H^{1}(\mathcal{B}), \ \zeta_{s}|_{\partial \mathcal{B}_{\theta_{s}}} = 0 \right\},$$

$$V_{\zeta_{f}} = \left\{ \zeta_{f} : \mathcal{B} \to \mathbb{R} \mid \zeta_{f} \in H^{1}(\mathcal{B}), \ \zeta_{f}|_{\partial \mathcal{B}_{\theta_{f}}} = 0 \right\},$$

$$V_{\omega} = \left\{ \omega : \mathcal{B} \to \mathbb{R} \mid \omega \in H^{1}(\mathcal{B}) \right\}.$$
(A.8)

Applying the standard weighted residual procedure, the weak statements for Eq. (A.1) is to: find $\{u, p_f, \theta_s, \theta_f, d\}$ $\in V_u \times V_p \times V_{\theta_s} \times V_{\theta_f} \times V_d$ such that for all $\{\eta, \xi, \zeta_s, \zeta_f, \omega\} \in V_{\eta} \times V_{\xi} \times V_{\zeta_s} \times V_{\zeta_f} \times V_{\omega}$,

$$G_u = G_p = G_{\theta_s} = G_d = 0,$$
 (A.9)

where:

e:
$$\begin{cases}
G_{u} = \int_{\mathcal{B}} \nabla \boldsymbol{\eta} : \boldsymbol{\sigma} \, dV - \int_{\mathcal{B}} \boldsymbol{\eta} \cdot \rho \boldsymbol{g} \, dV - \int_{\partial \mathcal{B}_{t}} \boldsymbol{\eta} \cdot \hat{\boldsymbol{t}} \, d\Gamma = 0, & \text{(a)} \\
G_{p} = \int_{\mathcal{B}} \xi \frac{1}{M^{*}} \dot{p}_{f} \, dV - \int_{\mathcal{B}} \xi \left[3\alpha_{s}(B^{*} - \phi^{f}) \right] \dot{\theta}_{s} \, dV \\
+ \int_{\mathcal{B}} \xi (B^{*}\nabla \cdot \boldsymbol{v}) \, dV - \int_{\mathcal{B}} \nabla \xi \cdot \boldsymbol{w} \, dV - \int_{\mathcal{B}} \xi \hat{\boldsymbol{s}} \, dV - \int_{\partial \mathcal{B}_{w}} \xi \hat{\boldsymbol{w}} \, d\Gamma = 0, & \text{(b)} \\
G_{\theta_{s}} = \int_{\mathcal{B}} \zeta_{s} \rho^{s} c_{s} \dot{\theta}_{s} \, dV - \int_{\mathcal{B}} \zeta_{s} \mathcal{D}_{\text{int}}^{s} \, dV - \int_{\mathcal{B}} \nabla \zeta_{s} \cdot \boldsymbol{q}^{s} \, dV \\
- \int_{\mathcal{B}} \zeta_{s} \hat{r}^{s} \, dV + \int_{\mathcal{B}} \zeta_{s} \left[a_{m} h_{m}(\theta_{s} - \theta_{f}) \right] dV - \int_{\partial \mathcal{B}_{q^{s}}} \zeta_{s} \hat{q}^{s} \, d\Gamma = 0, & \text{(c)} \\
G_{\theta_{f}} = \int_{\mathcal{B}} \zeta_{f}^{\text{SUPG}} \rho^{f} c_{f} \dot{\theta}_{f} \, dV + \int_{\mathcal{B}} \zeta_{f}^{\text{SUPG}} \rho_{f} c_{f} (\boldsymbol{w} \cdot \nabla \theta_{f}) \, dV - \int_{\mathcal{B}} \nabla \zeta_{f}^{\text{SUPG}} \cdot \boldsymbol{q}^{f} \, dV \\
- \int_{\mathcal{B}} \zeta_{f}^{\text{SUPG}} \hat{r}^{f} \, dV + \int_{\mathcal{B}} \zeta_{f} \left[a_{m} h_{m}(\theta_{f} - \theta_{s}) \right] dV - \int_{\partial \mathcal{B}_{q^{f}}} \zeta_{f} \hat{q}^{f} \, d\Gamma = 0, & \text{(d)} \\
G_{d} = \int_{\mathcal{B}} \omega g'(d) \mathcal{H} \, dV + \int_{\mathcal{B}} \omega d \, dV + \int_{\mathcal{B}} \nabla \omega \cdot (l_{c}^{2} \nabla \, d) \, dV = 0. & \text{(e)}
\end{cases}$$

Here, ζ_f^{SUPG} indicates the modified weighting function:

$$\zeta_f^{\text{SUPG}} = \zeta_f + \tau_{\text{SUPG}}(\boldsymbol{w} \cdot \nabla \zeta_f), \tag{A.11}$$

while τ_{SUPG} is the stabilization coefficient which is explicitly defined in Section 5.

A.2. Galerkin form

By letting N_u , N_p , N_s , N_f , and N_d be the shape function matrices for the displacement, pore pressure, solid temperature, fluid temperature, and phase field respectively; and η , ξ , ζ_s , ζ_f , and ω be the nodal values of the corresponding test functions, the following approximations are adopted:

$$\begin{cases} \boldsymbol{u} \approx \boldsymbol{u}^{h} = \mathbf{N}_{u} \mathbf{u} \\ p_{f} \approx p_{f}^{h} = \mathbf{N}_{p} \mathbf{p} \\ \theta_{s} \approx \theta_{s}^{h} = \mathbf{N}_{s} \mathbf{T}_{s} \\ \theta_{f} \approx \theta_{f}^{h} = \mathbf{N}_{f} \mathbf{T}_{f} \\ d \approx d^{h} = \mathbf{N}_{d} \mathbf{d} \end{cases}$$

$$\begin{cases} \boldsymbol{\eta} \approx \boldsymbol{\eta}^{h} = \mathbf{N}_{u} \boldsymbol{\eta} \\ \boldsymbol{\xi} \approx \boldsymbol{\xi}^{h} = \mathbf{N}_{p} \boldsymbol{\xi} \\ \boldsymbol{\xi}_{s} \approx \boldsymbol{\xi}_{s}^{h} = \mathbf{N}_{s} \boldsymbol{\xi}_{s} \\ \boldsymbol{\xi}_{f} \approx \boldsymbol{\xi}_{f}^{h} = \mathbf{N}_{f} \boldsymbol{\xi}_{f} \\ \boldsymbol{\omega} \approx \boldsymbol{\omega}^{h} = \mathbf{N}_{d} \boldsymbol{\omega} \end{cases}$$

$$(A.12)$$

and we define the following transformation matrices:

$$\mathbf{B}_{i} = \nabla \mathbf{N}_{i} \; ; \; \mathbf{b}_{i} = \nabla \cdot \mathbf{N}_{i} \; ; \; i = \{u, p, s, f, d\}. \tag{A.13}$$

Similarly, for the modified weighting function ζ_f^{SUPG} , we also define the following matrices:

$$\zeta_f^{\text{SUPG}} \approx \mathbf{N}_f^{\text{SUPG}} \zeta_f \; ; \; \mathbf{B}_f^{\text{SUPG}} = \nabla \; \mathbf{N}_f^{\text{SUPG}} \; ; \; \mathbf{b}_f^{\text{SUPG}} = \nabla \cdot \mathbf{N}_f^{\text{SUPG}}.$$
 (A.14)

Then, by following the standard procedure, we obtain the semi-discrete forms that we summarized in Eqs. (70)–(74), while the detailed expressions for all the vectors and matrices are as follows:

$$\begin{cases} \mathbf{K} = \int_{\mathcal{B}} \mathbf{b}_{\mathbf{u}}^{\mathsf{T}} \tilde{\mathbf{C}} \mathbf{B}_{\mathbf{u}} \, dV \\ \mathbf{G} = \int_{\mathcal{B}} \mathbf{b}_{\mathbf{u}}^{\mathsf{T}} B^{*} \mathbf{N}_{\mathbf{p}} \, dV \\ \mathbf{P} = \int_{\mathcal{B}} \mathbf{b}_{\mathbf{u}}^{\mathsf{T}} (3\alpha_{s} K^{*}) \mathbf{N}_{s} \, dV \\ \mathbf{P} = \int_{\mathcal{B}} \mathbf{b}_{\mathbf{u}}^{\mathsf{T}} (3\alpha_{s} K^{*}) \mathbf{N}_{s} \, dV \\ \mathbf{Q}_{\mathbf{f}} = \int_{\mathcal{B}} (\mathbf{N}_{\mathbf{f}}^{\mathsf{SUPG}})^{\mathsf{T}} \rho_{f} c_{f} \mathbf{w} \mathbf{B}_{\mathbf{f}} \, dV \\ \mathbf{Q}_{\mathbf{f}} = \int_{\mathcal{B}} (\mathbf{N}_{\mathbf{f}}^{\mathsf{SUPG}})^{\mathsf{T}} \rho_{f} c_{f} \mathbf{w} \mathbf{B}_{\mathbf{f}} \, dV \\ \mathbf{Q}_{\mathbf{f}} = \int_{\mathcal{B}} \mathbf{N}_{\mathbf{f}}^{\mathsf{T}} \frac{1}{M} \mathbf{N}_{\mathbf{f}} \, dV \\ \mathbf{Q}_{\mathbf{f}} = \int_{\mathcal{B}} \mathbf{N}_{\mathbf{f}}^{\mathsf{T}} a_{m} h_{m} \mathbf{N}_{\mathbf{f}} \, dV \\ \mathbf{E}_{\mathbf{f}} = \int_{\mathcal{B}} \mathbf{N}_{\mathbf{f}}^{\mathsf{T}} a_{m} h_{m} \mathbf{N}_{\mathbf{f}} \, dV \\ \mathbf{A} = \int_{\mathcal{B}} \mathbf{N}_{\mathbf{f}}^{\mathsf{T}} a_{m} h_{m} \mathbf{N}_{\mathbf{f}} \, dV \\ \mathbf{E}_{\mathbf{f}} = \int_{\mathcal{B}} \mathbf{N}_{\mathbf{f}}^{\mathsf{T}} a_{m} h_{m} \mathbf{N}_{\mathbf{f}} \, dV \\ \mathbf{A} = \int_{\mathcal{B}} \mathbf{N}_{\mathbf{f}}^{\mathsf{T}} a_{m} h_{m} \mathbf{N}_{\mathbf{f}} \, dV \\ \mathbf{E}_{\mathbf{f}} = \int_{\mathcal{B}} \mathbf{N}_{\mathbf{f}}^{\mathsf{T}} a_{m} h_{m} \mathbf{N}_{\mathbf{f}} \, dV \\ \mathbf{A} = \int_{\mathcal{B}} \mathbf{N}_{\mathbf{f}}^{\mathsf{T}} a_{m} h_{m} \mathbf{N}_{\mathbf{f}} \, dV \\ \mathbf{E}_{\mathbf{f}} = \int_{\mathcal{B}} \mathbf{N}_{\mathbf{f}}^{\mathsf{T}} a_{m} h_{m} \mathbf{N}_{\mathbf{f}} \, dV \\ \mathbf{E}_{\mathbf{f}} = \int_{\mathcal{B}} \mathbf{N}_{\mathbf{f}}^{\mathsf{T}} a_{m} h_{m} \mathbf{N}_{\mathbf{f}} \, dV \\ \mathbf{f}_{\mathbf{g}} = \int_{\partial \mathcal{B}_{\mathbf{g}}} \mathbf{N}_{\mathbf{f}}^{\mathsf{T}} a_{m} h_{m} \mathbf{N}_{\mathbf{f}} \, dV + \int_{\mathcal{B}} \mathbf{N}_{\mathbf{g}}^{\mathsf{T}} a_{\mathbf{f}} \, dV \\ \mathbf{f}_{\mathbf{g}} = \int_{\partial \mathcal{B}_{\mathbf{g}}} \mathbf{N}_{\mathbf{f}}^{\mathsf{T}} \hat{\mathbf{g}} \, dV + \int_{\mathcal{B}} \mathbf{N}_{\mathbf{f}}^{\mathsf{T}} \hat{\mathbf{g}} \, dV + \int_{\mathcal{B}} \mathbf{N}_{\mathbf{f}}^{\mathsf{T}} \hat{\mathbf{g}} \, dV + \int_{\mathcal{B}} \mathbf{N}_{\mathbf{f}}^{\mathsf{T}} a_{\mathbf{f}} \, dV \\ \mathbf{f}_{\mathbf{g}} = \int_{\partial \mathcal{B}_{\mathbf{g}}} \mathbf{N}_{\mathbf{f}}^{\mathsf{T}} \hat{\mathbf{g}} \, dV + \int_{\mathcal{B}} \mathbf{N}_{\mathbf{f}}^{\mathsf{T}} \hat{\mathbf{g}} \, dV + \int_{\mathcal{B}} \mathbf{N}_{\mathbf{f}}^{\mathsf{T}} \hat{\mathbf{g}} \, dV \\ \mathbf{f}_{\mathbf{g}} = \int_{\partial \mathcal{B}_{\mathbf{g}}} \mathbf{N}_{\mathbf{f}}^{\mathsf{T}} \hat{\mathbf{g}} \, dV + \int_{\mathcal{B}} \mathbf{N}_{\mathbf{f}}^{\mathsf{T}} \, dV + \int_{\mathcal{B}} \mathbf{N}_{\mathbf{f}}^{\mathsf{T}} \, dV + \int_{\mathcal{B}} \mathbf{N}_{\mathbf{f}}^{\mathsf{T}} \, dV +$$

where \tilde{C} indicates the tangential stiffness [i.e., matrix form of $g(d)\mathbb{C}^e$].

References

- [1] Hamed S Al-Hadhrami, Martin J Blunt, Thermally induced wettability alteration to improve oil recovery in fractured reservoirs, SPE Reserv. Eval. Eng. 4 (03) (2001) 179–186.
- [2] Ladislaus Rybach, Geothermal energy: sustainability and the environment, Geothermics 32 (4-6) (2003) 463-470.
- [3] Roland Pusch, Geological Storage of Highly Radioactive Waste: Current Concepts and Plans for Radioactive Waste Disposal, Springer Science & Business Media, 2009.
- [4] Richa Shukla, Pathegama Ranjith, Asadul Haque, Xavier Choi, A review of studies on CO2 sequestration and caprock integrity, Fuel 89 (10) (2010) 2651–2664.
- [5] Abdul Ravoof Shaik, Sheik S Rahman, Nam H Tran, Thanh Tran, Numerical simulation of fluid-rock coupling heat transfer in naturally fractured geothermal system, Appl. Therm. Eng. 31 (10) (2011) 1600–1606.
- [6] Zhenxue Dai, Hari Viswanathan, Richard Middleton, Feng Pan, William Ampomah, Changbing Yang, Wei Jia, Ting Xiao, Si-Yong Lee, Brian McPherson, et al., Co2 accounting and risk analysis for CO2 sequestration at enhanced oil recovery sites, Environ. Sci. Technol. 50 (14) (2016) 7546–7554.
- [7] WaiChing Sun, Zhijun Cai, Jinhyun Choo, Mixed arlequin method for multiscale poromechanics problems, Internat. J. Numer. Methods Engrg. 111 (7) (2017) 624–659.
- [8] Saeed Salimzadeh, Adriana Paluszny, Hamidreza M Nick, Robert W Zimmerman, A three-dimensional coupled thermo-hydro-mechanical model for deformable fractured geothermal systems, Geothermics 71 (2018) 212–224.
- [9] Bahador Bahmani, WaiChing Sun, A kd-tree-accelerated hybrid data-driven/model-based approach for poroelasticity problems with multi-fidelity multi-physics data, Comput. Methods Appl. Mech. Engrg. 382 (2021) 113868.
- [10] Eric C Bryant, WaiChing Sun, Phase field modeling of frictional slip with slip weakening/strengthening under non-isothermal conditions, Comput. Methods Appl. Mech. Engrg. 375 (2021) 113557.
- [11] James D Byerlee, Brittle-ductile transition in rocks, J. Geophys. Res. 73 (14) (1968) 4741-4750.

- [12] Mervyn S Paterson, Teng-fong Wong, Experimental Rock Deformation-the Brittle Field, Springer Science & Business Media, 2005.
- [13] Jinhyun Choo, WaiChing Sun, Coupled phase-field and plasticity modeling of geological materials: From brittle fracture to ductile flow, Comput. Methods Appl. Mech. Engrg. 330 (2018) 1–32.
- [14] Frank D Hansen, Christi D Leigh, Salt Disposal of Heat-Generating Nuclear Waste, Sandia National Laboratories, Albuquerque, NM, 2011
- [15] SeonHong Na, WaiChing Sun, Computational thermomechanics of crystalline rock, part I: A combined multi-phase-field/crystal plasticity approach for single crystal simulations, Comput. Methods Appl. Mech. Engrg. 338 (2018) 657–691.
- [16] Ran Ma, WaiChing Sun, Computational thermomechanics for crystalline rock. Part II: Chemo-damage-plasticity and healing in strongly anisotropic polycrystals, Comput. Methods Appl. Mech. Engrg. 369 (2020) 113184.
- [17] Jonny Rutqvist, Status of the TOUGH-FLAC simulator and recent applications related to coupled fluid flow and crustal deformations, Comput. Geosci. 37 (6) (2011) 739–750.
- [18] Olaf Kolditz, Sebastian Bauer, Lars Bilke, Norbert Böttcher, Jens-Olaf Delfs, Thomas Fischer, Uwe J Görke, Thomas Kalbacher, Georg Kosakowski, CI McDermott, et al., Opengeosys: an open-source initiative for numerical simulation of thermo-hydro-mechanical/chemical (THM/C) processes in porous media, Environ. Earth Sci. 67 (2) (2012) 589–599.
- [19] I Nozad, RG Carbonell, S Whitaker, Heat conduction in multiphase systems—I: theory and experiment for two-phase systems, Chem. Eng. Sci. 40 (5) (1985) 843–855.
- [20] I Nozad, RG Carbonell, S Whitaker, Heat conduction in multiphase systems—II: Experimental method and results for three-phase systems, Chem. Eng. Sci. 40 (5) (1985) 857–863.
- [21] DF McTigue, Thermoelastic response of fluid-saturated porous rock, J. Geophys. Res.: Solid Earth 91 (B9) (1986) 9533–9542.
- [22] M Kurashige, A thermoelastic theory of fluid-filled porous materials, Int. J. Solids Struct. 25 (9) (1989) 1039–1052.
- [23] RW Zimmerman, Coupling in poroelasticity and thermoelasticity, Int. J. Rock Mech. Min. Sci. 37 (1-2) (2000) 79-87.
- [24] Anastasia Belotserkovets, Jean H Prevost, Thermoporoelastic response of a fluid-saturated porous sphere: An analytical solution, Internat. J. Engrg. Sci. 49 (12) (2011) 1415–1423.
- [25] WaiChing Sun, A stabilized finite element formulation for monolithic thermo-hydro-mechanical simulations at finite strain, Internat. J. Numer. Methods Engrg. 103 (11) (2015) 798–839.
- [26] SeonHong Na, WaiChing Sun, Computational thermo-hydro-mechanics for multiphase freezing and thawing porous media in the finite deformation range, Comput. Methods Appl. Mech. Engrg. 318 (2017) 667–700.
- [27] Jihoon Kim, Unconditionally stable sequential schemes for all-way coupled thermoporomechanics: Undrained-adiabatic and extended fixed-stress splits, Comput. Methods Appl. Mech. Engrg. 341 (2018) 93–112.
- [28] Nima Noii, Thomas Wick, A phase-field description for pressurized and non-isothermal propagating fractures, Comput. Methods Appl. Mech. Engrg. 351 (2019) 860–890.
- [29] HV Truong, Go E Zinsmeister, Experimental study of heat transfer in layered composites, Int. J. Heat Mass Transfer 21 (7) (1978) 905–909.
- [30] L-W He, Z-H Jin, Y Zhang, Convective cooling/heating induced thermal stresses in a fluid saturated porous medium undergoing local thermal non-equilibrium, Int. J. Solids Struct. 49 (5) (2012) 748–758.
- [31] Fangming Jiang, Jiliang Chen, Wenbo Huang, Liang Luo, A three-dimensional transient model for EGS subsurface thermo-hydraulic process, Energy 72 (2014) 300–310.
- [32] M Quintard, M Kaviany, S Whitaker, Two-medium treatment of heat transfer in porous media: numerical results for effective properties, Adv. Water Resour. 20 (2–3) (1997) 77–94.
- [33] CT Hsu, A closure model for transient heat conduction in porous media, 1999.
- [34] WJ Minkowycz, A Haji-Sheikh, KF Vafai, On departure from local thermal equilibrium in porous media due to a rapidly changing heat source: the sparrow number, Int. J. Heat Mass Transfer 42 (18) (1999) 3373–3385.
- [35] Akira Nakayama, Fujio Kuwahara, Masazumi Sugiyama, Guoliang Xu, A two-energy equation model for conduction and convection in porous media, Int. J. Heat Mass Transfer 44 (22) (2001) 4375–4379.
- [36] JG Fourie, JP Du Plessis, A two-equation model for heat conduction in porous media (i: Theory), Transp. Porous Media 53 (2) (2003) 145–161.
- [37] JG Fourie, JP Du Plessis, A two-equation model for heat conduction in porous media (ii: application), Transp. Porous Media 53 (2) (2003) 163–174.
- [38] L Virto, M Carbonell, R Castilla, Pedro Javier Gamez-Montero, Heating of saturated porous media in practice: several causes of local thermal non-equilibrium, Int. J. Heat Mass Transfer 52 (23–24) (2009) 5412–5422.
- [39] Thomas JR Hughes, Michel Mallet, Mizukami Akira, A new finite element formulation for computational fluid dynamics: II. beyond SUPG, Comput. Methods Appl. Mech. Engrg. 54 (3) (1986) 341–355.
- [40] Thomas JR Hughes, Leopoldo P Franca, Gregory M Hulbert, A new finite element formulation for computational fluid dynamics: VIII. The Galerkin/least-squares method for advective-diffusive equations, Comput. Methods Appl. Mech. Engrg. 73 (2) (1989) 173–189.
- [41] Jinhyun Choo, WaiChing Sun, Cracking and damage from crystallization in pores: Coupled chemo-hydro-mechanics and phase-field modeling, Comput. Methods Appl. Mech. Engrg. 335 (2018) 347–379.
- [42] Christian Miehe, Martina Hofacker, Fabian Welschinger, A phase field model for rate-independent crack propagation: Robust algorithmic implementation based on operator splits, Comput. Methods Appl. Mech. Engrg. 199 (45–48) (2010) 2765–2778.
- [43] Michael J Borden, Clemens V Verhoosel, Michael A Scott, Thomas JR Hughes, Chad M Landis, A phase-field description of dynamic brittle fracture, Comput. Methods Appl. Mech. Engrg. 217 (2012) 77–95.
- [44] Hyoung Suk Suh, WaiChing Sun, Devin T. O'Connor, A phase field model for cohesive fracture in micropolar continua, Comput. Methods Appl. Mech. Engrg. (ISSN: 0045-7825) 369 (2020) 113181, http://dx.doi.org/10.1016/j.cma.2020.113181, URL http://www.sciencedirect.com/science/article/pii/S0045782520303662.

- [45] Christian Miehe, Steffen Mauthe, Phase field modeling of fracture in multi-physics problems. Part iii. crack driving forces in hydro-poro-elasticity and hydraulic fracturing of fluid-saturated porous media, Comput. Methods Appl. Mech. Engrg. 304 (2016) 619–655.
- [46] Yehuda Bachmat, Jacob Bear, Macroscopic modelling of transport phenomena in porous media. 1: The continuum approach, Transp. Porous Media 1 (3) (1986) 213–240.
- [47] Olivier Coussy, Luc Dormieux, Emmanuel Detournay, From mixture theory to Biot's approach for porous media, Int. J. Solids Struct. 35 (34–35) (1998) 4619–4635.
- [48] Luc Dormieux, Djimédo Kondo, Franz-Josef Ulm, Microporomechanics, John Wiley & Sons, 2006.
- [49] William G Gray, A derivation of the equations for multi-phase transport, Chem. Eng. Sci. 30 (2) (1975) 229–233.
- [50] A Amiri, K Vafai, TM Kuzay, Effects of boundary conditions on non-Darcian heat transfer through porous media and experimental comparisons, Numer. Heat Transf. A: Appl. 27 (6) (1995) 651–664.
- [51] B Alazmi, K Vafai, Analysis of fluid flow and heat transfer interfacial conditions between a porous medium and a fluid layer, Int. J. Heat Mass Transfer 44 (9) (2001) 1735–1749.
- [52] Ray M Bowen, Incompressible porous media models by use of the theory of mixtures, Internat. J. Engrg. Sci. 18 (9) (1980) 1129–1148.
- [53] Olgierd C Zienkiewicz, AHC Chan, M Pastor, BA Schrefler, T Shiomi, Computational Geomechanics, Vol. 613, Citeseer, 1999.
- [54] Wolfgang Ehlers, Foundations of multiphasic and porous materials, in: Porous Media, Springer, 2002, pp. 3-86.
- [55] Olivier Coussy, Poromechanics, John Wiley & Sons, 2004.
- [56] Reint De Boer, Theory of Porous Media: Highlights in Historical Development and Current State, Springer Science & Business Media, 2012.
- [57] Matthias Preisig, Jean H Prévost, Coupled multi-phase thermo-poromechanical effects. Case study: CO2 injection at In Salah, Algeria, Int. J. Greenh. Gas Control 5 (4) (2011) 1055–1064.
- [58] J. Rutqvist, L. Börgesson, M. Chijimatsu, A. Kobayashi, L. Jing, T.S. Nguyen, J. Noorishad, C.-F. Tsang, Thermohydromechanics of partially saturated geological media: governing equations and formulation of four finite element models, Int. J. Rock Mech. Min. Sci. (ISSN: 1365-1609) 38 (1) (2001) 105–127, http://dx.doi.org/10.1016/S1365-1609(00)00068-X, URL https://www.sciencedirect.com/science/article/pii/S136516090000068X, Decovalex II.
- [59] SeonHong Na, WaiChing Sun, Wave propagation and strain localization in a fully saturated softening porous medium under the non-isothermal conditions, Int. J. Numer. Anal. Methods Geomech. 40 (10) (2016) 1485–1510.
- [60] N Khalili, A Uchaipichat, AA Javadi, Skeletal thermal expansion coefficient and thermo-hydro-mechanical constitutive relations for saturated homogeneous porous media, Mech. Mater. 42 (6) (2010) 593–598.
- [61] Blaise Bourdin, Gilles A Francfort, Jean-Jacques Marigo, The variational approach to fracture, J. Elasticity 91 (1-3) (2008) 5-148.
- [62] David Bryant Mumford, Jayant Shah, Optimal approximations by piecewise smooth functions and associated variational problems, Comm. Pure Appl. Math. (1989).
- [63] JD Clayton, J Knap, Phase field modeling of twinning in indentation of transparent crystals, Modelling Simulation Mater. Sci. Eng. 19 (8) (2011) 085005.
- [64] A Mesgarnejad, B Bourdin, MM3340163 Khonsari, Validation simulations for the variational approach to fracture, Comput. Methods Appl. Mech. Engrg. 290 (2015) 420–437.
- [65] Jeremy Bleyer, Roberto Alessi, Phase-field modeling of anisotropic brittle fracture including several damage mechanisms, Comput. Methods Appl. Mech. Engrg. 336 (2018) 213–236.
- [66] Gilles A Francfort, J-J Marigo, Revisiting brittle fracture as an energy minimization problem, J. Mech. Phys. Solids 46 (8) (1998) 1319–1342.
- [67] Eric Lorentz, A nonlocal damage model for plain concrete consistent with cohesive fracture, Int. J. Fract. 207 (2) (2017) 123-159.
- [68] Rudy JM Geelen, Yingjie Liu, Tianchen Hu, Michael R Tupek, John E Dolbow, A phase-field formulation for dynamic cohesive fracture, Comput. Methods Appl. Mech. Engrg. 348 (2019) 680–711.
- [69] Hyoung Suk Suh, WaiChing Sun, An open-source fenics implementation of a phase field fracture model for micropolar continua, Int. J. Multiscale Comput. Eng. 17 (6) (2019).
- [70] M Dittmann, F Aldakheel, J Schulte, F Schmidt, M Krüger, P Wriggers, C Hesch, Phase-field modeling of porous-ductile fracture in non-linear thermo-elasto-plastic solids, Comput. Methods Appl. Mech. Engrg. 361 (2020) 112730.
- [71] Ronaldo I Borja, On the mechanical energy and effective stress in saturated and unsaturated porous continua, Int. J. Solids Struct. 43 (6) (2006) 1764–1786.
- [72] Ronaldo I Borja, Azad Koliji, On the effective stress in unsaturated porous continua with double porosity, J. Mech. Phys. Solids 57 (8) (2009) 1182–1193.
- [73] Qiang Yang, Laurent Stainier, Michael Ortiz, A variational formulation of the coupled thermo-mechanical boundary-value problem for general dissipative solids, J. Mech. Phys. Solids 54 (2) (2006) 401–424.
- [74] Christian Miehe, M Hofacker, L-M Schänzel, Fadi Aldakheel, Phase field modeling of fracture in multi-physics problems. Part ii. coupled brittle-to-ductile failure criteria and crack propagation in thermo-elastic-plastic solids, Comput. Methods Appl. Mech. Engrg. 294 (2015) 486–522.
- [75] Maurice A Biot, General theory of three-dimensional consolidation, J. Appl. Phys. 12 (2) (1941) 155–164.
- [76] O Vincké, P Longuemare, M Boutéca, JP Deflandre, et al., Investigation of the poromechanical behavior of shales in the elastic domain, in: SPE/ISRM Rock Mechanics in Petroleum Engineering, Society of Petroleum Engineers, 1998.
- [77] John Conrad Jaeger, Neville GW Cook, Robert Zimmerman, Fundamentals of Rock Mechanics, John Wiley & Sons, 2009.
- [78] Steffen Mauthe, Christian Miehe, Hydraulic fracture in poro-hydro-elastic media, Mech. Res. Commun. 80 (2017) 69-83.
- [79] Seong Jun Ha, Jinhyun Choo, Tae Sup Yun, Liquid CO 2 fracturing: Effect of fluid permeation on the breakdown pressure and cracking behavior, Rock Mech. Rock Eng. 51 (11) (2018) 3407–3420.

- [80] Yousef Heider, WaiChing Sun, A phase field framework for capillary-induced fracture in unsaturated porous media: Drying-induced vs. hydraulic cracking, Comput. Methods Appl. Mech. Engrg. 359 (2020) 112647.
- [81] VA Lubarda, On thermodynamic potentials in linear thermoelasticity, Int. J. Solids Struct. 41 (26) (2004) 7377–7398.
- [82] M Dittmann, M Krüger, F Schmidt, S Schuß, C Hesch, Variational modeling of thermomechanical fracture and anisotropic frictional mortar contact problems with adhesion, Comput. Mech. 63 (3) (2019) 571–591.
- [83] Rachel Gelet, Benjamin Loret, Nasser Khalili, A thermo-hydro-mechanical coupled model in local thermal non-equilibrium for fractured HDR reservoir with double porosity, J. Geophys. Res.: Solid Earth 117 (B7) (2012).
- [84] Clifford Truesdell, Richard Toupin, The classical field theories, in: Principles of Classical Mechanics and Field Theory/Prinzipien Der Klassischen Mechanik Und Feldtheorie, Springer, 1960, pp. 226–858.
- [85] Ralph Abraham, Jerrold E Marsden, Jerrold E Marsden, Foundations of Mechanics, Vol. 36, Benjamin/Cummings Publishing Company Reading, Massachusetts, 1978.
- [86] Gerhard A Holzapfel, Nonlinear solid mechanics: a continuum approach for engineering science, Meccanica 37 (4) (2002) 489-490.
- [87] JC Simo, Ch Miehe, Associative coupled thermoplasticity at finite strains: Formulation, numerical analysis and implementation, Comput. Methods Appl. Mech. Engrg. 98 (1) (1992) 41–104.
- [88] Felipe T Dórea, Marcelo JS De Lemos, Simulation of laminar impinging jet on a porous medium with a thermal non-equilibrium model, Int. J. Heat Mass Transfer 53 (23–24) (2010) 5089–5101.
- [89] A Gandomkar, KE Gray, Local thermal non-equilibrium in porous media with heat conduction, Int. J. Heat Mass Transfer 124 (2018) 1212–1216.
- [90] Thomas Heinze, Possible effect of flow velocity on thawing rock-water-ice systems under local thermal non-equilibrium conditions, Cold Regions Sci. Technol. 170 (2020) 102940.
- [91] Kim Pham, Jean-Jacques Marigo, From the onset of damage to rupture: construction of responses with damage localization for a general class of gradient damage models, Contin. Mech. Thermodyn. 25 (2) (2013) 147–171.
- [92] Morton E Gurtin, Generalized Ginzburg-Landau and cahn-hilliard equations based on a microforce balance, Physica D 92 (3–4) (1996) 178–192
- [93] Zachary A Wilson, Michael J Borden, Chad M Landis, A phase-field model for fracture in piezoelectric ceramics, Int. J. Fract. 183 (2) (2013) 135–153.
- [94] Christian Miehe, Fabian Welschinger, Martina Hofacker, Thermodynamically consistent phase-field models of fracture: Variational principles and multi-field FE implementations, Internat. J. Numer. Methods Engrg. 83 (10) (2010) 1273–1311.
- [95] Hanen Amor, Jean-Jacques Marigo, Corrado Maurini, Regularized formulation of the variational brittle fracture with unilateral contact: Numerical experiments, J. Mech. Phys. Solids 57 (8) (2009) 1209–1229.
- [96] RJ Atkin, RE Craine, Continuum theories of mixtures: basic theory and historical development, Quart. J. Mech. Appl. Math. 29 (2) (1976) 209–244.
- [97] Jean H Prévost, Mechanics of continuous porous media, Internat. J. Engrg. Sci. 18 (6) (1980) 787-800.
- [98] WaiChing Sun, Jakob T Ostien, Andrew G Salinger, A stabilized assumed deformation gradient finite element formulation for strongly coupled poromechanical simulations at finite strain, Int. J. Numer. Anal. Methods Geomech. 37 (16) (2013) 2755–2788.
- [99] Ronaldo I Borja, Enrique Alarcón, A mathematical framework for finite strain elastoplastic consolidation part 1: Balance laws, variational formulation, and linearization, Comput. Methods Appl. Mech. Engrg. 122 (1–2) (1995) 145–171.
- [100] Jean H Prevost, Nonlinear transient phenomena in saturated porous media, Comput. Methods Appl. Mech. Engrg. 30 (1) (1982) 3–18.
- [101] M Necati Özışık, Boundary Value Problems of Heat Conduction, courier Corporation, 1989.
- [102] A Amiri, Kambiz Vafai, Analysis of dispersion effects and non-thermal equilibrium, non-darcian, variable porosity incompressible flow through porous media, Int. J. Heat Mass Transfer 37 (6) (1994) 939–954.
- [103] Changho Lee, Hyoung Suk Suh, Boyeong Yoon, Tae Sup Yun, Particle shape effect on thermal conductivity and shear wave velocity in sands, Acta Geotech. 12 (3) (2017) 615–625.
- [104] Hyoung Suk Suh, Kwang Yeom Kim, Junhwan Lee, Tae Sup Yun, Quantification of bulk form and angularity of particle with correlation of shear strength and packing density in sands, Eng. Geol. 220 (2017) 256–265.
- [105] Hyoung Suk Suh, Tae Sup Yun, Modification of capillary pressure by considering pore throat geometry with the effects of particle shape and packing features on water retention curves for uniformly graded sands, Comput. Geotech. 95 (2018) 129–136.
- [106] Yousef Heider, Hyoung Suk Suh, WaiChing Sun, An offline multi-scale unsaturated poromechanics model enabled by self-designed/self-improved neural networks, Int. J. Numer. Anal. Methods Geomech. (2021).
- [107] Stephen Whitaker, Simultaneous heat, mass, and momentum transfer in porous media: a theory of drying, in: Advances in Heat Transfer, Vol. 13, Elsevier, 1977, pp. 119–203.
- [108] KD Pennell, 2.5 Specific Surface Area, Methods Soil Anal.: Part 4 Phys. Methods 5 (2002) 295-315.
- [109] Gan Feng, Yong Kang, Xiao-chuan Wang, Fracture failure of granite after varied durations of thermal treatment: an experimental study, R. Soc. Open Sci. 6 (7) (2019) 190144.
- [110] Gan Feng, Xiao-chuan Wang, Yong Kang, Shi-gang Luo, Yao-qing Hu, Effects of temperature on the relationship between mode-I fracture toughness and tensile strength of rock, Appl. Sci. 9 (7) (2019) 1326.
- [111] Zachary A Wilson, Chad M Landis, Phase-field modeling of hydraulic fracture, J. Mech. Phys. Solids 96 (2016) 264–290.
- [112] Kun Wang, WaiChing Sun, A unified variational eigen-erosion framework for interacting brittle fractures and compaction bands in fluid-infiltrating porous media, Comput. Methods Appl. Mech. Engrg. 318 (2017) 1–32.
- [113] Yousef Heider, Sönke Reiche, Philipp Siebert, Bernd Markert, Modeling of hydraulic fracturing using a porous-media phase-field approach with reference to experimental data, Eng. Fract. Mech. 202 (2018) 116–134.
- [114] Chukwudi Chukwudozie, Blaise Bourdin, Keita Yoshioka, A variational phase-field model for hydraulic fracturing in porous media, Comput. Methods Appl. Mech. Engrg. 347 (2019) 957–982.

- [115] Wai Ching Sun, Jose E Andrade, John W Rudnicki, Multiscale method for characterization of porous microstructures and their impact on macroscopic effective permeability, Internat. J. Numer. Methods Engrg. 88 (12) (2011) 1260–1279.
- [116] WaiChing Sun, José E Andrade, John W Rudnicki, Peter Eichhubl, Connecting microstructural attributes and permeability from 3D tomographic images of in situ shear-enhanced compaction bands using multiscale computations, Geophys. Res. Lett. 38 (10) (2011).
- [117] Hyoung Suk Suh, Dong Hun Kang, Jaewon Jang, Kwang Yeom Kim, Tae Sup Yun, Capillary pressure at irregularly shaped pore throats: Implications for water retention characteristics, Adv. Water Resour. 110 (2017) 51–58.
- [118] WaiChing Sun, Teng-fong Wong, Prediction of permeability and formation factor of sandstone with hybrid lattice Boltzmann/finite element simulation on microtomographic images, Int. J. Rock Mech. Min. Sci. 106 (2018) 269–277.
- [119] John R Booker, Thermal convection with strongly temperature-dependent viscosity, J. Fluid Mech. 76 (4) (1976) 741-754.
- [120] Emmanuel O Egbogah, Jack T Ng, An improved temperature-viscosity correlation for crude oil systems, J. Pet. Sci. Eng. 4 (3) (1990) 197–200.
- [121] BS Bhadauria, Palle Kiran, Heat transport in an anisotropic porous medium saturated with variable viscosity liquid under temperature modulation, Transp. Porous Media 100 (2) (2013) 279–295.
- [122] Stephen G Brush, Theories of liquid viscosity, Chem. Rev. 62 (6) (1962) 513-548.
- [123] Robert C Reid, John M Prausnitz, Bruce E Poling, The Properties of Gases and Liquids, McGraw Hill Book Co., New York, NY, 1987.
- [124] Lawrence Korson, Walter Drost-Hansen, Frank J Millero, Viscosity of water at various temperatures, J. Phys. Chem. 73 (1) (1969) 34–39.
- [125] GQ Tang, NR Morrow, Temperature Salinity, Oil composition, and oil recovery by waterflooding, SPE Reserv. Eng. 12 (04) (1997) 269–276.
- [126] P Smolinski, T Belytschko, M Neal, Multi-time-step integration using nodal partitioning, Internat. J. Numer. Methods Engrg. 26 (2) (1988) 349–359.
- [127] WJT Daniel, Analysis and implementation of a new constant acceleration subcycling algorithm, Internat. J. Numer. Methods Engrg. 40 (15) (1997) 2841–2855.
- [128] Ernst Rank, Casimir Katz, Heinrich Werner, On the importance of the discrete maximum principle in transient analysis using finite element methods, Internat. J. Numer. Methods Engrg. 19 (12) (1983) 1771–1782.
- [129] HR Thomas, Z Zhou, Minimum time-step size for diffusion problem in FEM analysis, Internat. J. Numer. Methods Engrg. 40 (20) (1997) 3865–3880.
- [130] W Cui, KA Gawecka, DMG Taborda, DM Potts, L Zdravković, Time-step constraints in transient coupled finite element analysis, Internat. J. Numer. Methods Engrg. 106 (12) (2016) 953–971.
- [131] Wentao Li, Changfu Wei, Minimum time-step size in transient finite element analysis of coupled poromechanical problems, Comput. Geotech. 98 (2018) 197–204.
- [132] Timo Heister, Mary F Wheeler, Thomas Wick, A primal-dual active set method and predictor-corrector mesh adaptivity for computing fracture propagation using a phase-field approach, Comput. Methods Appl. Mech. Engrg. 290 (2015) 466–495.
- [133] S Teichtmeister, D Kienle, F Aldakheel, M-A Keip, Phase field modeling of fracture in anisotropic brittle solids, Int. J. Non-Linear Mech. 97 (2017) 1–21.
- [134] KC Park, Partitioned transient analysis procedures for coupled-field problems: stability analysis, 1980.
- [135] TS Nguyen, APS Selvadurai, Coupled thermal-mechanical-hydrological behaviour of sparsely fractured rock: implications for nuclear fuel waste disposal, Int. J. Rock Mech. Min. Sci. Geomech. Abstr. 32 (1995) 465–479, Elsevier.
- [136] Sanghyun Lee, Mary F Wheeler, Thomas Wick, Pressure and fluid-driven fracture propagation in porous media using an adaptive finite element phase field model, Comput. Methods Appl. Mech. Engrg. 305 (2016) 111–132.
- [137] E Turska, BA Schrefler, On convergence conditions of partitioned solution procedures for consolidation problems, Comput. Methods Appl. Mech. Engrg. 106 (1–2) (1993) 51–63.
- [138] T Belytschko, Wing K Liu, P Smolinksi, Multi-stepping implicit-explicit procedures in transient analysis, in: Innovative Methods in Nonlinear Analysis, Pineridge Press, 1984, pp. 135–154.
- [139] Anthony Gravouil, Alain Combescure, Multi-time-step explicit—implicit method for non-linear structural dynamics, Internat. J. Numer. Methods Engrg. 50 (1) (2001) 199–225.
- [140] Tayfun E Tezduyar, YJ Park, Discontinuity-capturing finite element formulations for nonlinear convection-diffusion-reaction equations, Comput. Methods Appl. Mech. Engrg. 59 (3) (1986) 307–325.
- [141] Tayfun E Tezduyar, Stabilized finite element formulations for incompressible flow computations, Adv. Appl. Mech. 28 (1991) 1-44.
- [142] Murad AbuAisha, Benjamin Loret, Stabilization of forced heat convection: applications to enhanced geothermal systems (EGS), Transp. Porous Media 112 (1) (2016) 229–252.
- [143] J Lemonds, A Needleman, Finite element analyses of shear localization in rate and temperature dependent solids, Mech. Mater. 5 (4) (1986) 339–361.
- [144] Comput Miehe, Entropic thermoelasticity at finite strains. Aspects of the formulation and numerical implementation, Comput. Methods Appl. Mech. Engrg. 120 (3–4) (1995) 243–269.
- [145] Patrick Erbts, Alexander DüSter, Accelerated staggered coupling schemes for problems of thermoelasticity at finite strains, Comput. Math. Appl. 64 (8) (2012) 2408–2430.
- [146] P Smolinski, S Sleith, T Belytschko, Stability of an explicit multi-time step integration algorithm for linear structural dynamics equations, Comput. Mech. 18 (3) (1996) 236–244.
- [147] PA Vermeer, A Verruijt, An accuracy condition for consolidation by finite elements, Int. J. Numer. Anal. Methods Geomech. 5 (1) (1981) 1–14.

- [148] Jihoon Kim, Hamdi A Tchelepi, Ruben Juanes, et al., Stability, accuracy and efficiency of sequential methods for coupled flow and geomechanics, in: SPE Reservoir Simulation Symposium, Society of Petroleum Engineers, 2009.
- [149] Gilbert Strang, Gilbert Strang, Gilbert Strang, Gilbert Strang, Introduction to Linear Algebra, Vol. 3, Wellesley-Cambridge Press Wellesley, MA, 1993.
- [150] Lloyd N Trefethen, David Bau III, Numerical Linear Algebra, Vol. 50, Siam, 1997.
- [151] Ilja N Bronshtein, Konstantin A Semendyayev, Handbook of Mathematics, Springer Science & Business Media, 2013.
- [152] W Michael Lai, David H Rubin, David Rubin, Erhard Krempl, Introduction to Continuum Mechanics, Butterworth-Heinemann, 2009.
- [153] R Liu, MF Wheeler, CN Dawson, R Dean, Modeling of convection-dominated thermoporomechanics problems using incomplete interior penalty Galerkin method, Comput. Methods Appl. Mech. Engrg. 198 (9–12) (2009) 912–919.
- [154] Robert J Plemmons, M-matrix characterizations. I—nonsingular M-matrices, Linear Algebra Appl. 18 (2) (1977) 175–188.
- [155] Takao Fujimoto, Ravindra Ranade, Two characterizations of inverse-positive matrices: the hawkins-simon condition and the Le Chatelier-Braun principle, Electron. J. Linear Algebra 11 (2004).
- [156] Anders Logg, Garth N Wells, Dolfin: Automated finite element computing, ACM Trans. Math. Softw. 37 (2) (2010) 1-28.
- [157] Anders Logg, Kent-Andre Mardal, Garth Wells, Automated Solution of Differential Equations by the Finite Element Method: The FEniCS Book, Vol. 84, Springer Science & Business Media, 2012.
- [158] Martin Alnæs, Jan Blechta, Johan Hake, August Johansson, Benjamin Kehlet, Anders Logg, Chris Richardson, Johannes Ring, Marie E Rognes, Garth N Wells, The fenics project version 1.5, Arch. Numer. Softw. 3 (100) (2015).
- [159] Shrirang Abhyankar, Jed Brown, Emil M Constantinescu, Debojyoti Ghosh, Barry F Smith, Hong Zhang, Petsc/TS: A modern scalable ODE/DAE solver library, 2018, arXiv preprint arXiv:1806.01437.